



THE HONG KONG
POLYTECHNIC UNIVERSITY

香港理工大學

Pao Yue-kong Library

包玉剛圖書館

Copyright Undertaking

This thesis is protected by copyright, with all rights reserved.

By reading and using the thesis, the reader understands and agrees to the following terms:

1. The reader will abide by the rules and legal ordinances governing copyright regarding the use of the thesis.
2. The reader will use the thesis for the purpose of research or private study only and not for distribution or further reproduction or any other purpose.
3. The reader agrees to indemnify and hold the University harmless from and against any loss, damage, cost, liability or expenses arising from copyright infringement or unauthorized usage.

IMPORTANT

If you have reasons to believe that any materials in this thesis are deemed not suitable to be distributed in this form, or a copyright owner having difficulty with the material being included in our database, please contact lbsys@polyu.edu.hk providing details. The Library will look into your claim and consider taking remedial action upon receipt of the written requests.

NANOMANUFACTURING OF PLASMONIC
MATERIALS FOR SENSING APPLICATIONS

CHEUNG TAI-LOK

M.Phil

The Hong Kong Polytechnic University

2017

The Hong Kong Polytechnic
University

Department of Industrial and Systems Engineering

Nanomanufacturing of Plasmonic Materials for
Sensing Applications

Cheung Tai-Lok

A thesis submitted in partial fulfilment of the requirements for
the

Degree of Master of Philosophy

June 2016

CERTIFICATE OF ORIGINALITY

I hereby declare that this thesis is my own work and that, to the best of my knowledge and belief, it reproduces no material previously published or written, nor material that has been accepted for the award of any other degree or diploma, except where due acknowledgement has been made in the text.

_____ (Signed)

_____ Cheung Tai-Lok _____ (Name of student)

Abstract

In this thesis, a new approach for manufacturing novel plasmonic nanomaterials (i.e. Copper sulfide nanocrystals (Cu_{2-x}S NCs)) for sensing applications has been developed. Unlike the traditional plasmonic nanomaterials (e.g. gold nanoparticles and nanorods), in which the plasmon resonance is supported by the collection of surface free electrons, the plasmonic features of Cu_{2-x}S NCs are originated from the copious free holes. Those varied free holes act as the charge carriers and allow for the condition of plasmon resonance. This condition is very sensitive to the dielectric surrounding of nanocrystals, and thus Cu_{2-x}S NC can serve as a sensing substrate. Indeed, the sensitivity of this plasmonic substrate is governed by several factors (i.e. size, morphology and nonstoichiometric compositions (number of free hole) of nanocrystals). However, there is little empirical research can be found for the synthesis of Cu_{2-x}S NCs with controlled size, morphology and nonstoichiometric compositions. Some modification techniques have been developed. The main drawbacks were the incorporation of toxic surfactants and the sophisticated preparation procedures. This study presents a non-toxic and efficient approach for the synthesis of Cu_{2-x}S NCs. Furthermore, their plasmonic properties and sensing capability were also studied.

Firstly, a continuous-flow millifluidic device for synthesizing different morphologies and nonstoichiometric compositions of Cu_{2-x}S NCs is presented. The device is polydimethylsiloxane (PDMS)- based, fabricated using a three-dimensional (3D) printer followed by moulding with PDMS. This millifluidic device acted as a nanomanufacturing platform and offered an ideal incubation environment, such as

uniform heating, higher production rate, precise control on the distribution between precursors and the reaction time for incubation, for the growth of NCs,.

The as-synthesized Cu_{2-x}S NCs were characterized by the scanning transmission electron microscope (STEM) and powder X-ray diffraction (XRD). It has shown that through the control of the input flow rates, it was manageable to fabricate spherical Cu_{2-x}S NCs with diameter 3.6 – 12.6 nm and rod-shaped Cu_{2-x}S NCs with aspect ratio 2.3 – 3.4. In addition, by altering the molar ratios between precursors, it was able to fabricate four different nonstoichiometric compositions of Cu_{2-x}S NCs including $\text{Cu}_{1.1}\text{S}$, $\text{Cu}_{1.39}\text{S}$, $\text{Cu}_{1.75}\text{S}$ and $\text{Cu}_{1.97}\text{S}$.

Secondly, we present an investigation of sensing capability of Cu_{2-x}S NCs by varying the refractive index around the NCs surfaces. The shift of the localized surface plasmon resonance (LSPR) of Cu_{2-x}S NCs was measured due to the change of refractive index in the media. It has been shown that different sized Cu_{2-x}S NCs have a range of sensitivity from 573 nm / RIU to 850 nm / RIU. Similarly, different aspect ratios of the rod-shaped Cu_{2-x}S NCs have shown a change of sensitivity from 714 nm / RIU to 985 nm / RIU. For the nonstoichiometric compositions of Cu_{2-x}S NCs, the delivered range of response was 386 nm / RIU to 714 nm / RIU. Furthermore, a plasmonic quenching effect was proposed and demonstrated by the use of o-phenyldiamine (OPD). OPD is a compound which emitted yellow fluorescence (568 nm) when it was oxidized (electrons donator) by the Cu_{2-x}S NCs (electrons acceptor). As the concentration of OPD increased, more Cu_{2-x}S NCs were quenched and the fluorescence was enhanced, therefore the plasmonic quenching effect could be observed. It was shown that the LSPR of Cu_{2-x}S NCs was quenched effectively as the ratio of Cu_{2-x}S NCs to OPD increased from 0.003 to 600. Besides, the

fluorescence was enhanced from 0.2×10^3 to 1.1×10^6 by distinct morphologies and compositions of Cu_{2-x}S NCs. All Cu_{2-x}S NCs / OPD samples showed that the enhancement was optimized when the ratio reached 0.3. The results showed a satisfying signal-to-noise ratio and sensing capability, revealing the potential for the future development of the Cu_{2-x}S NCs based nanosensor.

List of Publications

1. L. Hong, **T.-L. Cheung**, C. Dang, P. H. J. Chong, L. Liu, W.-C. Law and K.-T. Yong, Millifluidic Synthesis of Cadmium Sulfide Nanoparticles and Its Application in Bioimaging. *RSC Advances* **2017**. (In press) (The underlined authors share the first authorship)
2. C. H. Ng; N. Rao; W. C. Law; G. Xu; **T. L. Cheung**; F. T. Cheng; H. C. Man, Enhancing the cell proliferation performance of NiTi substrate by laser diffusion nitriding. *Surface and Coatings Technology* **2016**, 309, 59-66.
3. W. C. Law, **T. L. Cheung**, N. Rao, 3D-printed millifluidic chip for synthesising plasmonic semiconductor nanocrystals as sensors substrate. *HKIE Transactions* **2016**, 23(4), 174-178. (awarded paper)
4. Z. Xu; N. Rao; **T.-L. Cheung**; C. Y. Tang; C.-P. Tsui; W. C. Law, *Preparation of Thermal-Responsive Polymeric Nanocapsules for Controlled Release of Therapeutic*. The Twenty-fourth Annual International Conference on COMPOSITES/NANO ENGINEERING (ICCE-24), ICCE-24 Haikou, Hainan Island, China, July 17-23, 2016.
5. **T.-L. Cheung**; L. Hong; N. Rao; C. Yang; L. Wang; W. J. Lai; P. H. J. Chong; W.-C. Law; K.-T. Yong, The non-aqueous synthesis of shape controllable Cu_{2-x}S plasmonic nanostructures in a continuous-flow millifluidic chip for the generation of photo-induced heating. *Nanoscale* **2016**, 8 (12), 6609-6622.

Acknowledgements

I wish to express my sincere appreciation to my chief supervisor, Dr. Wing Cheung, Roy, Law, who always supports and provides valuable advice. His encouragement motivated me to have better performance. Without his guidance and persistent help, this dissertation would not have been possible.

I wish also like to express my gratitude to Prof. Benny C.F. Cheung and Dr. C.H. Cheng for always supporting me and discussing different issues concerning the project. Their suggestions on research direction and methodology were so helpful for me.

I also wish to thank to my friends in my research group, Ms. Nanxi Rao, Mr. Zhou Rui Xu and my Department as well. I am so happy to meet them during my research study. Thank you for sharing happiness and sorrow with me.

Besides, I would like to express my heartfelt thanks to my family members and my fiancée. Thank you for supporting me for my study. Thank you for their endless love to me. I also like to say thank you to my friends for accompanying me when I felt alone and confused during me study.

Table of Contents

Abstract	i
List of Publications	iv
Acknowledgements	v
Table of Contents	vi
List of Figures	viii
List of Tables.....	xi
Chapter 1 Introduction	1
1.1 Background of Study	1
1.2 Purposes of Study.....	3
1.3 Significance of Investigation	4
1.4 Objectives.....	5
1.5 Dissertation Structure.....	5
Chapter 2 Literature Review	7
2.1 Traditional Non-Plasmonic Sensing Techniques using Semiconductor Copper Sulfide Nanocrystals.....	7
2.1.1 Electrochemical Sensing Technique	8
2.1.2 Chemiluminescence Sensing Technique.....	9
2.2 Current Plasmonic Sensing Technique using Metallic Nanocrystals	10
2.2.1 Shift of LSPR Peaks.....	10
2.2.2 Fluorescence Quenching / Enhancement by Metallic Nanocrystals	12
2.2.3 Raman Resonance	13
2.3 Existing Challenges of the Plasmonic Sensing Technique for Semiconductor Cu_{2-x}S Nanocrystals.....	14
2.3.1 Morphologies and Compositions Control of Cu_{2-x}S NCs	14
2.3.2 Plasmonic Properties of Cu_{2-x}S NCs	15
2.4 Suggested Approaches from Literature.....	18
2.4.1 Synthesis of Cu_{2-x}S NCs using Millifluidic Device	18
2.4.2 Development of New Sensing Mechanism.....	23
Chapter 3 Methodology.....	27
3.1 Morphologies and Compositions Control of Cu_{2-x}S NCs by Millifluidic Device	27

3.1.1	Design and Fabrication of Millifluidic Device	27
3.1.2	Synthetic Setting for Cu _{2-x} S NCs Fabrication	31
3.1.3	Material and Characterization Method.....	33
3.2	A Study on the Plasmonic Properties of a variety of Morphologies and Compositions of Cu _{2-x} S NCs	34
3.2.1	Organic Solvent.....	35
3.2.2	Aqueous Environment.....	36
3.3	A Study on the Plasmonic Quenching and the Fluorescence Enhancement for the Sensing Mechanism Development.....	37
Chapter 4 Results and Discussion		40
4.1	Characterization of the Cu _{2-x} S NCs Fabricated by Millifluidic Device	40
4.1.1	Morphology Modification.....	40
4.1.2	Composition Modification	46
4.1.3	LSPR Spectra of the Cu _{2-x} S NCs by Varying Different Flow Rates and Precursors' Concentration.....	52
4.2	The Results of the Plasmonic Property in a variety of Morphologies and Compositions of Cu _{2-x} S NCs	55
4.2.1	Organic Environment	55
4.2.2	Aqueous Environment.....	56
4.3	Plasmonic Quenching Effect and the Fluorescence Enhancement by Different Ratios between Cu _{2-x} S NCs and OPD in a Variety of Morphologies and Compositions of the Cu _{2-x} S NCs	59
4.3.1	Plasmonic Quenching Effect.....	60
4.3.2	Fluorescence Enhancement.....	66
Chapter 5 Conclusions and Future Work		73
References		77

List of Figures

Figure 1 Size-dependent LSPR frequency by 60nm diameter and 30nm diameter AuNPs, respectively.....	11
Figure 2 Adjustable LSPR frequency (from NIR to FIR) by the level of doping of a semiconductor nanocrystal.....	16
Figure 3 Typical setting up of a bench-top synthesis environment. Various temperature profiles are found due to different inputs from reflux condenser, inert gas, heating mantel and stirring bar etc.....	19
Figure 4 Uniform heating incubation environment from the continuous flow microfluidic channel device demonstrated by Zhao et al. [61].....	21
Figure 5 Continuous flow microreactor for AuNP synthesis designed and performed by Catherine J. Murphy et al. [66].	21
Figure 6 Refractive index dependence plasmonic property of Cu_{2-x}S NCs reported by Liu et al. [6].....	23
Figure 7 Size dependence plasmonic property of Cu_{2-x}S NCs revealed by Luther et al. [2].....	24
Figure 8 Composition dependence plasmonic property of Cu_{2-x}S NCs demonstrated by Burda et al. [1].....	25
Figure 9 (a) 3D printed ABS mould for the PDMS millifluidic device (b) Top view of the PDMS millifluidic device. (c) Schematic description of nanoparticles fabrication in the continuous-flow millifluidic device (d) Nanoparticles fabrication in PDMS millifluidic device.	29
Figure 10 Schematic diagram on the plasmonic quenching and the fluorescence enhancement by the use of o-phenyldiamine (OPD) to the Cu_{2-x}S NCs.....	38
Figure 11 Fluorescence intensity of various concentrations of oxidized o-phenyldiamine (OPDox) in pure water.	39
Figure 12 TEM images for different morphologies of Cu_{2-x}S NCs. Distinct morphologies of Cu_{2-x}S NCs were modified by varying the flow rates and precursor concentration in the millifluidic device.....	42
Figure 13 TEM images of Cu_{2-x}S NCs exhibiting different morphologies synthesized at flow rates of (a) $150 \mu\text{l min}^{-1}$, (b) $1000 \mu\text{l min}^{-1}$, (c) $2000 \mu\text{l min}^{-1}$, (i) $3000 \mu\text{l min}^{-1}$, (j) $4000 \mu\text{l min}^{-1}$ and (k) $5000 \mu\text{l min}^{-1}$, and their respective size distributions (d, e, f, l, m and n) and aspect ratios (g, h, o, p and q). The precursors' concentration between Cu : S kept at 1 : 2.	44
Figure 14 TEM images of Cu_{2-x}S NCs synthesizing at different precursors' concentration of Cu : S for (a) 1 : 10, (b) 1 : 6, (c) 1 : 2, (j) 2 : 1, (k) 6 : 1 and (l) 10 : 1, exhibiting different morphologies and their respective size distributions (d, e, f, m, n and o) and aspect ratios (g, h, i, p, q and r). The flow rate was set at $3000 \mu\text{l min}^{-1}$...	45

Figure 15 XRD patterns for the modification of the compositions of Cu_{2-x}S NCs by varying precursors' concentrations. a) covellite $\text{Cu}_{1.1}\text{S}$ (PDF Card 01-078-2391) b) roxbyite $\text{Cu}_{1.75}\text{S}$ (PDF Card 00-0232-0958) and djurleite $\text{Cu}_{1.97}\text{S}$ (PDF Card 00-020-0365)	49
Figure 16 XRD patterns for the modification of the compositions of Cu_{2-x}S NCs by varying the flow rates of the precursors. a) covellite $\text{Cu}_{1.1}\text{S}$ (PDF Card 01-078-2391) and b) spionkopite $\text{Cu}_{1.39}\text{S}$ (PDF Card 00-036-0380)	49
Figure 17 HRTEM images of individual nanoparticle with different compositions of covellite (a and c), djurleite (e and g), roxbyite (i) and spionkopite (k), and the corresponding FFT analysis for covellite (b and d), djurleite (f and h), roxbyite (j) and spionkopite (l).....	50
Figure 18 Rietveld refinement XRD fitting for different Cu_{2-x}S NCs sample data – A) 1:2 (Cu:S) molar ratio with 1000 $\mu\text{l}/\text{min}$ flow rate B) 2:1 (Cu:S) molar ratio with 3000 $\mu\text{l}/\text{min}$. Blue curve shows the fitted Rietveld refinement profiles and the red curve shows the measured data. The corresponding difference plots between the fitted data and the measured data are also included respectively.....	50
Figure 19 EDX measurements for Cu_{2-x}S NCs using different precursor's concentration.	51
Figure 20 Absorption spectra of the Cu_{2-x}S NCs by varying a) different flow rates and b) precursors' concentration.	54
Figure 21 Responses of the LSPR peaks Cu_{2-x}S NCs upon different organic solvents with a ranged of refractive index.	55
Figure 22 The effect of a variety of glycerin-water ratios to the LSPR peaks by different a) sizes b) aspect ratios and c) compositions of Cu_{2-x}S NCs.....	57
Figure 23 Digital photos on different ratios between Cu_{2-x}S NCs (ppm) and the OPD (ppm) started from the leftmost (0 : 21600), (650 : 21600), (650 : 10800), (650 : 216) and (650 : 0).	59
Figure 24 Plasmonic quenching of different sized spherical $\text{Cu}_{1.39}\text{S}$ NCs for a) 3.6 nm b) 6.4 nm and c) 12.6 nm. The black line indicates the 65 ppm spherical $\text{Cu}_{1.39}\text{S}$ NCs. The following red, light blue, green, purple, light brown, navy blue and dark brown lines indicates different OPD (ppm) amount from 0.108, 1.08, 10.8, 21.6, 216, 2160 and 21600 respectively.....	61
Figure 25 Plasmonic quenching of different aspect ratios of the rod-shaped $\text{Cu}_{1.1}\text{S}$ NCs for a) 1.1 b) 2.3 and c) 3.4. The black line indicates the 65 ppm rod-shaped $\text{Cu}_{1.1}\text{S}$ NCs. The following red, light blue, green, purple, light brown, navy blue and dark brown lines indicates different OPD (ppm) amount from 0.108, 1.08, 10.8, 21.6, 216, 2160 and 21600 respectively.....	62
Figure 26 Plasmonic quenching of different compositions of the 8.8 nm spherical Cu_{2-x}S NCs for a) $\text{Cu}_{1.1}\text{S}$ b) $\text{Cu}_{1.39}\text{S}$ c) $\text{Cu}_{1.75}\text{S}$ and d) $\text{Cu}_{1.97}\text{S}$. The black line indicates the 65 ppm rod-shaped Cu_{2-x}S NCs. The following red, light blue, green, purple, light brown, navy blue and dark brown lines indicates different OPD (ppm) amount from 0.108, 1.08, 10.8, 21.6, 216, 2160 and 21600 respectively.....	64

Figure 27 Enhanced fluorescence intensity under different size spherical $\text{Cu}_{1.39}\text{S}$ NCs for a) 3.6 nm b) 6.4 nm and c) 12.6 nm. The black, red, blue, green, purple, light brown and the navy blue lines indicate different ratios of $\text{Cu}_{1.39}\text{S}$ NCs to OPD ranging from 600, 60, 6, 3, 0.3, 0.03 and 0.003, respectively..... 68

Figure 28 Enhanced fluorescence intensity under different aspect ratios of the rod-shaped $\text{Cu}_{1.1}\text{S}$ NCs for a) 1.1 b) 2.3 and c) 3.4. The black, red, blue, green, purple, light brown and the navy blue lines indicate different ratios of $\text{Cu}_{1.39}\text{S}$ NCs to OPD ranging from 600, 60, 6, 3, 0.3, 0.03 and 0.003, respectively..... 69

Figure 29 Enhanced fluorescence intensity of different compositions of the 8.8 nm spherical Cu_{2-x}S NCs for a) $\text{Cu}_{1.1}\text{S}$ b) $\text{Cu}_{1.39}\text{S}$ c) $\text{Cu}_{1.75}\text{S}$ and d) $\text{Cu}_{1.97}\text{S}$. The black, red, blue, green, purple, light brown and the navy blue lines indicate different ratios of $\text{Cu}_{1.39}\text{S}$ NCs to OPD ranging from 600, 60, 6, 3, 0.3, 0.03 and 0.003, respectively. . 71

List of Tables

Table 1 Summary of the morphologies, compositions and plasmonic absorption peaks of Cu_{2-x}S NCs by varying different flow rates and the copper to sulfur molar ratios.....	43
Table 2 EDX composition ratios compared against the XRD fittings.....	51
Table 3 The LSPR peaks shifted per each percentage of glycerin-water ratio and the refractive index unit (RIU) of different a) size b) aspect ratios and c) compositions of Cu_{2-x}S NCs by a variety of glycerin-water ratios.....	58
Table 4 Plasmonic quenching effect on different sized spherical $\text{Cu}_{1.39}\text{S}$ NCs by measuring the intensity of the LSPR peaks under a variety of OPD amount.	64
Table 5 Plasmonic quenching effect on different aspect ratios of the rod-shaped $\text{Cu}_{1.1}\text{S}$ NCs by measuring the intensity of the LSPR peaks under a variety of OPD amount.....	65
Table 6 Plasmonic quenching effect on different compositions of the 8.8 nm spherical Cu_{2-x}S NCs by measuring the intensity of the LSPR peaks under a variety of OPD amount.	65
Table 7 Enhanced fluorescence intensity on different sized spherical $\text{Cu}_{1.39}\text{S}$ NCs by measuring the intensity of the fluorescence peaks at 568 nm under a variety of OPD amount.....	71
Table 8 Enhanced fluorescence intensity on different aspect ratios of the rod-shaped $\text{Cu}_{1.1}\text{S}$ NCs by measuring the intensity of the fluorescence peaks at 568 nm under a variety of OPD amount.	72
Table 9 Enhanced fluorescence intensity on different compositions of the 8.8 nm spherical Cu_{2-x}S NCs by measuring the intensity of the fluorescence peaks at 568 nm under a variety of OPD amount.	72

Chapter 1 Introduction

1.1 Background of Study

In recent years, the world's population multiplied more rapidly than any in historical records before, more people are living in a high dense area, the potential threats such as food safety, drinking water safety, air pollution and the spread of communicable diseases are getting tremendous public concern. It is necessary to take action in early stages to keep those potential threats. As an earlier and effective detection can greatly reduce the severity of the events, it is important to develop a fast, accurate and ultra-sensitive point-of-care monitoring sensors for monitoring public healthcare. This could not only allow a better preparation for the public protection but also strengthen our crisis management efficiency and effectiveness.

The performance of a sensor is mainly determined by its sensing mechanism. Over the several decades, many researchers have developed several of sensing techniques. One of the promising approaches is the use of plasmonic nanoparticle as a sensing substrate. The main reason for plasmonic-based sensors to become a powerful tool in sensing applications is their capability of fast detection and ultrasensitive detection. In this type of sensor, plasmonic is the confined oscillation of free electrons on metal surface, normally gold and silver. When there is an incident light coming to those nanoparticles, the oscillation of free electrons leads to strong absorbance and scattering of light. The absorbance and the scattering can be altered by the change of the size and shape of the nanoparticles and its surrounding refractive index. The plasmonic sensor exploits this sensing mechanism through the interaction between the sensing analyte and the nanoparticles and obtaining the changes of its optical

properties. However, there are still some unsatisfactory performances in detecting small molecules (e.g. DNA and virus). The relatively high development cost of the gold and silver nanoparticles also becomes one of the largest obstacles for wide applications.

In order to address these issues, this dissertation has studied recently developed plasmonic material, copper-based semiconductor nanocrystal. This novel plasmonic material has drawn attention of many researchers since its resonant property is governed by another mechanism, which is known as oscillation of free holes. The free holes act as charge carriers that provide mobility for the oscillation of the plasmonics. Since the density of the charge carriers can be altered (10^{17} cm^{-3} to 10^{22} cm^{-3}) by different levels of doping, it is worth studying the relationship between the doping concentration and the sensitivity of the semiconductor nanocrystals towards the surrounding environment. Moreover, since copper is an abundant element in earth, the development cost of the copper-based semiconductor nanocrystals can be potentially reduced.

Experiments were carried out to show this novel plasmonic sensing mechanism using copper-based semiconductor nanocrystals and thereby benefit the public health development in our community.

1.2 Purposes of Study

The purpose of this dissertation is to study the plasmonic sensing using semiconductor nanocrystals. The highly self-doped copper sulfide nanocrystals (Cu_{2-x}S NCs) was selected as the plasmonic material. The plasmonic property of the Cu_{2-x}S NCs was firstly proposed and studied in 2009 by Burda's group [1]. It has observed a strong near infrared absorption in Cu_{2-x}S NCs, and suggested that was contributed by the localized surface plasmon resonance (LSPR) of free holes in the valence band. Since then, many research works started to study the LSPR property of the Cu_{2-x}S NCs [2-8]. Those studies have further strengthened the correlation between the plasmonic properties and the number of holes in the valence band of the semiconductor Cu_{2-x}S NCs. The adjustable vacancies of the semiconductor nanocrystals offer an additional capability comparing to the metallic nanoparticles, which has a fixed electron carrier density. However, very few studies were focused on the sensing capability of Cu_{2-x}S NCs. This was because there are challenges on the synthesis of different morphologies and compositions of the Cu_{2-x}S NCs. Taking metallic nanocrystals as an example, it is well-known that different morphology and the composition exhibited different plasmonic behavior [9]. As a result, there are three purposes in this study. The first one is to fabricate different morphologies and compositions of Cu_{2-x}S NCs. The second is to study the plasmonic properties with different size, shape and crystal compositions of Cu_{2-x}S NCs. The third is to evaluate the sensing capability using the new plasmonic sensing mechanism.

1.3 Significance of Investigation

With the discovery of the heavily-doped p-type Cu_{2-x}S NCs by Burda's and Luther's group since 2009 [1, 2], heavily-doped Cu_{2-x}S NCs brought a promising advance in the field of plasmonic sensing. Typically, metallic nanocrystals only exploited its electrons to sense the surrounding media. The novel heavily-doped Cu_{2-x}S NCs utilize the free carriers (free holes) for the sensing application. Free carries of Cu_{2-x}S NCs not only possess the similar reactivity to the surrounding as metallic nanocrystals do, but also easily altered by the target analyte. This could provide enormous potential in ultrasensitive device development.

However, most of the recent studies were focusing on the relationship between the number of holes of Cu_{2-x}S NCs and its corresponding plasmonic properties, while little empirical research, for investigating the effect of morphologies and nonstoichiometric compositions. This might be attributed to the lack of effective ways for the control of the morphologies and the compositions of the Cu_{2-x}S NCs. One of the common approaches for the modification involved the highly toxic surfactant, trioctylphosphine oxide (TOPO) [10]. The significance of this study is firstly to demonstrate the fabrication of different morphologies and compositions of Cu_{2-x}S NCs using a millifluidic device, followed by examining the plasmonic properties of Cu_{2-x}S NCs with different morphologies and compositions. It is expected that the research findings in this study can provide a better understanding on the behavior of plasmonic semiconductor nanocrystals, establishing a fundamental study for the development of ultra-sensitive point-of-care device using new sensing mechanism.

1.4 Objectives

1. To synthesize the heavily-doped semiconductor Cu_{2-x}S NCs by injection approach.
2. To modify the morphologies and chemical compositions of the Cu_{2-x}S NCs using a continuous millifluidic device.
3. To study the plasmonic properties of Cu_{2-x}S NCs in two different circumstances
a) change of refractive index and b) plasmonic quenching effect.

1.5 Dissertation Structure

This dissertation is organized as follows: Chapter 1 Introduction: It includes research background, research purposes, significance and the objectives of this study.

Chapter 2 Literature Review: It firstly introduces the overview of the traditional sensing mechanism using non-plasmonic semiconductor nanocrystals. Secondly, it summarizes the current plasmonic sensing technique using metallic nanocrystals. Thirdly, this chapter identifies the existing research gap in plasmonic behavior study of Cu_{2-x}S NCs.

Chapter 3 Methodology: It demonstrates the control of shape, size and composition of Cu_{2-x}S NCs using continuous flow millifluidic device, which is called as nanomanufacturing device. Secondly, it introduces the approaches for the study of plasmonic quenching and fluorescence enhancement.

Chapter 4 Results and Discussion: It includes the characterization of different morphologies and compositions of Cu_{2-x}S NCs. After that, it provides the plasmonic behavior of Cu_{2-x}S NCs under different refractive index environment. Thirdly, this

chapter is to present the plasmonic quenching effect and the fluorescence enhancement under different morphologies and compositions Cu_{2-x}S NCs.

Chapter 5 Conclusions and Future Work: It summarizes the works done in the study. In addition, it also suggests two different approaches for the nanomanufacturing platform and the possible study on Surface-Enhanced Raman Scattering (SERS) by Cu_{2-x}S NCs.

Chapter 2 Literature Review

2.1 Traditional Non-Plasmonic Sensing Techniques using Semiconductor Copper Sulfide Nanocrystals

The semiconductor copper sulfide nanocrystals were traditionally used in non-plasmonic sensing technique. This technique was applied in sensing biological substances such as DNA, glucose and protein and gas substances such as ethanol, ammonia and hydrogen sulfide gas. Copper sulfide nanocrystals acted as an electron acceptor that received the electrons transferred from the analyte, resulting in the decrease of number of holes. The decrease of number of holes was then recorded in terms of resistance increase or the change of cyclic voltammetry potential. Examples and the detailed mechanism will be introduced in the following parts.

2.1.1 Electrochemical Sensing Technique

Electrochemical sensing is widely applied in different kinds of analyte such as glucose [11-21], hydrogen peroxide [22-24], hydroquinone [25] and pentachlorophenol [26]. This technique usually involves two detection techniques which are the cyclic voltammetry (CV) and the amperometry detection. CV analysis is usually conducted in advance since it is used to determine the largest response of the potential change with different analyte amount. After deciding the largest response potential, amperometry detection is conducted under this potential for further measurement such as sensitivity and detection limit on the analyte. Typically, during the assay, copper sulfide nanocrystals acted as an electron acceptor. When the analyte reacted with the nanocrystals, the Cu (II) ions in the nanocrystals were oxidized and formed Cu (I) ions by the process of direct electro-oxidation. This reaction increased the anodic peak current proportionally to the number of the analyte. However, this technique is limited by the resolution of the amperometry device, which is typically achieved to micro-ampere level.

2.1.2 Chemiluminescence Sensing Technique

The chemiluminescence is another sensing technique which has been applied on DNA [27-29], single nucleotide polymorphism (SNP) [30], ammonia gas [31-34] and adenosine triphosphate (ATP) [35]. The luminescence is attributed by the fluorescence dye such as luminol. In general, the dye was firstly labeled on the analyte, on the other hand, the probe for the analyte was conjugated to the copper sulfide nanocrystals. When the analyte reacted with the probe, the copper ions in the nanocrystals are released and excited the fluorescence of the dye. Although this approach could achieve a relative high resolution (since the resolution of the photoluminescence reading normally achieved 0.5nm), typical examples of this approach had a weak fluorescence intensity with only hundreds of intensity [27, 35]. This might be attributed to the relative weak oxidizing power of copper sulfide nanocrystals, since the nanocrystals were synthesized with a relative large diameter of hundreds of nanometer, so that the plasmonic effect was not significant.

2.2 Current Plasmonic Sensing Technique using Metallic Nanocrystals

It is well-known that metallic nanocrystals such as gold nanoparticle and silver nanoparticle are excellent plasmonic nanosensor with a relative rich carrier density (10^{23} cm^{-3}). Metallic nanocrystals exploit their abundant electrons to perform excellent sensing application. Metallic nanocrystals highly sensitive to any slight change of surrounding dielectric medium such as refractive index and overlapping of the plasmonics field. Despite that the electron carrier density of metallic nanocrystals are fixed, their rich carrier density have been exploited and performed well in plasmonic sensing through the shift of localized surface plasmonic resonance (LSPR) peaks, fluorescence quenching or enhancement and Raman resonance application.

2.2.1 Shift of LSPR Peaks

When it comes to a nanoscale sized particle, the surface plasmonics are confined to oscillate at a specific frequency. As the incident light resonates with the surface plasmonics, the plasmonics absorb or scatter the particular frequency of light. Since the energy spectrum in nanoparticles is discrete, the bandgap becomes size-dependent. Therefore, the absorption spectrum exhibits blue-shift for a smaller nanoparticle. A typical example was demonstrated by Chen et al. [36], the functionalized gold nanorod was used as the immunosensor probe for neuron cell. The original LSPR peaks of nanorod were 522 nm and 782 nm, for its lateral and longitudinal emission. When it conjugated with the anti-neuron specific enolase substance, the LSPR were slightly shifted to 532 nm and 757 nm. In the presence of neuron cell, the LSPR showed a significant 40 nm blue shift in longitudinal part and 15 nm red shift in lateral part. The color of the gold nanorod was altered from red

color to bluish violet, indicating that the shifting of the LSPR peaks. The LSPR shifting could be applied in the plasmonic sensing.

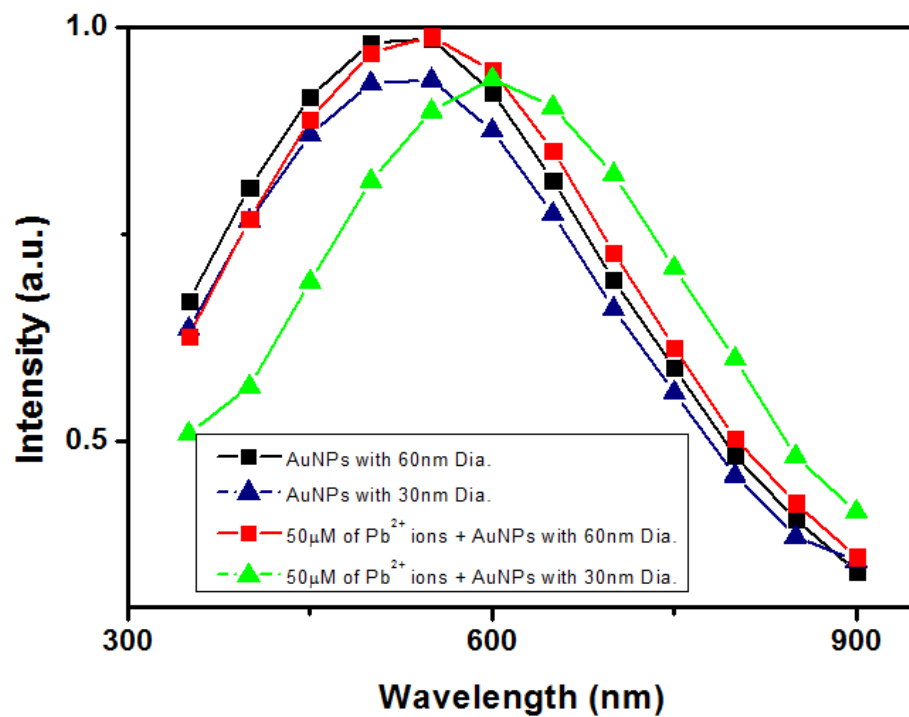


Figure 1 Size-dependent LSPR frequency by 60nm diameter and 30nm diameter AuNPs, respectively.

2.2.2 Fluorescence Quenching / Enhancement by Metallic Nanocrystals

Since metallic nanocrystals contain high electron carrier density, it can perform as excellent fluorescence quenchers. In the fluorescence quenching / enhancement mechanism, gold nanoparticles act as electron donor, while the fluorophore acts as electron receptor. Since the plasmonics of the metallic nanoparticles oscillated in a spherical range of 50 nm and according to the inverse-square law, the longer of the conjugates would reduce the quenching / enhancement efficiency [37]. Samanta et al. [37] have conducted the fluorescence quenching efficiency between the quantum dot (electron receptor) and the gold nanoparticle (electron donor). The gold nanoparticles were first modified with large number of DNA origami surfactant, which was used to control the interparticle distance. They have shown that when the interparticle distance decreased from 69.8 nm to 14.7 nm, the fluorescence intensity was quenched to its original 20% intensity. On the other hand, as removing the gold nanoparticle from the quantum dot, the fluorescence from the quantum dot has emitted again. This technique was powerful in sensing mechanism.

2.2.3 Raman Resonance

Raman Resonance is another technique in plasmonic sensing. In general, Raman spectroscopy is a technique to measure the inelastic scattering of light. The inelastic scattering refers to the change of the frequency of the photons of light, which is either being absorbed (stokes) or enhanced (anti-stokes). When there was an electron-rich or plasmonic-rich metallic nanoparticle existed, the Raman signal could be enhanced which was known as surface enhanced Raman scattering (SERS). SERS could be further strengthened by increasing the curvature of nanoparticles. Tian's group [38] have demonstrated that SERS signal of gold nanostar was stronger than gold nanotriangle and nanosphers. Tuan et al. [39] also discovered similar enhancement when the number of branches of nanoparticles increases, the SERS intensity also strengthened. Another approach for the SERS signal enhancement was through the aggregation of nanoparticles. Since the aggregated nanoparticles caused the overlapping of electric fields, so that a stronger resonant took place. This overlapping region was known as "hot spot". One of the representative example was conducted by Wustholz et al. [40], who have demonstrated the aggregated induced "hot spot" actually boosted the SERS signal up to two orders of magnitude.

2.3 Existing Challenges of the Plasmonic Sensing Technique for Semiconductor Cu_{2-x}S Nanocrystals

2.3.1 Morphologies and Compositions Control of Cu_{2-x}S NCs

Shape, size and composition are significant to the plasmonic properties of Cu_{2-x}S NCs. As mentioned before, gold nanorod have exhibited two LSPR peaks, while gold nanosphere only exhibited one peak [41]. Irregular shape of nanoparticles could enhance the Raman signal dramatically [42]. Larger sized nanoparticles had red-shift in LSPR, while smaller sized one have blue-shift [43]. Different compositions also brought different LSPR responses, the copper-deficient nanocrystals would perform blue-shift than the copper-rich compositions [2]. However, there were few studies on the shape and size control of Cu_{2-x}S NCs. One of the reports was done by Kruszynska et al. [44], who have demonstrated to control the Cu_{2-x}S nanorods with lengths ranged from 10 to 100 nm, However, this protocol involved a toxic reducing agent, which was Trioctylphosphine oxide (TOPO). TOPO had been confirmed harmful to the biological substances and the environment [10], which were the adverse effect as a sensing probe. Xie et al. [45] have successfully performed the size control on Cu_{2-x}S nanodisks by deploying different molar ratios between the surfactants. However, this approach could only manage size control, but not the crystal structures as all the samples were covellite structure ($\text{Cu}_{1.1}\text{S}$). Another work performed by Liu et al. [6] also only managed to control the size of Cu_{2-x}S NCs through the adjustment of aging time, but did not mention too much in the control of crystal structure and compositions of Cu_{2-x}S NCs.

2.3.2 Plasmonic Properties of Cu_{2-x}S NCs

Another challenge is the study of the plasmonic properties of different morphologies and compositions / crystal structure of Cu_{2-x}S NCs. Although there were some studies that demonstrated the LSPR properties of Cu_{2-x}S NCs, the literature on its plasmonic properties showed a lack of comprehensiveness. Cu_{2-x}S NCs was confirmed as a plasmonic material by Burda's group [1] and Alivisatos' group [2] in 2009 and 2011 respectively. Cu_{2-x}S NCs is a heavily doped (p-type) plasmonic semiconductor nanocrystals and exhibits strong NIR LSPRs, which is stoichiometry-dependent, size-dependent and sensitive to surrounding medium as shown in Figure 2. Alivisatos' group has further developed a mathematic calculation to describe the relationship between the LSPR frequency and the carrier density [2] as follow:

$$\text{LSPR frequency} = \frac{1}{2\pi} \sqrt{\frac{Ne^2}{\epsilon_0 m_e (\epsilon_\infty + 2\epsilon_m)}}$$

Where

- ϵ_∞ refers to the high frequency dielectric constant and assumed to be 10;
- ϵ_m refers to the medium dielectric constant and assumed as 2.25 for toluene solvent;
- m_e refers to the effective mass of the free carrier and assumed as a free electron;
- e refers to the electronic charge and
- ϵ_0 refers to the permittivity of free space.

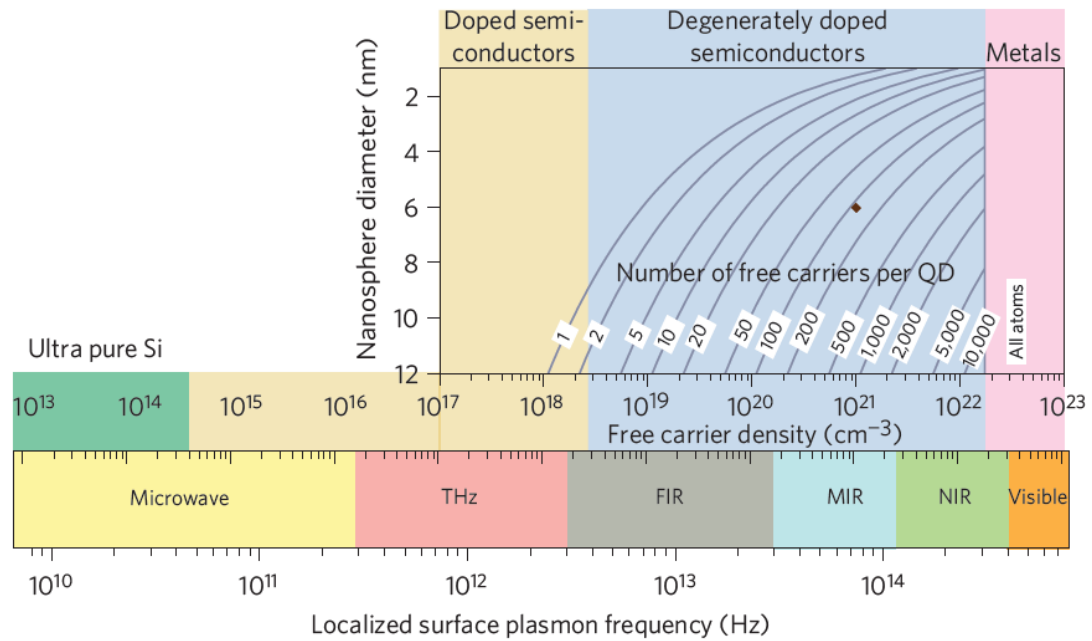


Figure 2 Adjustable LSPR frequency (from NIR to FIR) by the level of doping of a semiconductor nanocrystal.

After that, Kriegel et al. [3] have demonstrated the reversible tuning of the LSPR peaks for Cu_{2-x}S NCs by oxidizing, which was a typical way to increase the number of free hole in a heavily-doped p-type semiconductor NCs. Hsu et al. [4] have further investigated the effects on the carrier density of the disk-like Cu_{2-x}S NCs. They have purposed that the blue-shift of LSPR peaks was tuned by the oxidation or increased the number of holes of Cu_{2-x}S NCs. Wei et al. [5] also suggested that the reversible tuning LSPR peaks could be accomplished by loading / unloading surface ligand, which could trap the holes of the Cu_{2-x}S NCs and induced almost 130 nm shifting. Liu et al. [6] have also studied the tuning ability of LSPR peaks by dispersing the Cu_{2-x}S NCs into different refractive index solvents. In addition, Manna's group [7] have also demonstrated the quenching ability of Cu_{2-x}S NCs. LSPR peak vanished by adding Cu(I) complex ($[\text{Cu}(\text{CH}_3\text{CN})_4]\text{PF}_6$) as an electron donor, which was used to filled up the holes in the Cu_{2-x}S NCs. Recently, Alam et al. [8] have successfully demonstrated the holes trapping activity by adding methyl viologen radicals. Methyl

viologen was oxidized by Cu_{2-x}S NCs and transferred electron to trap the holes in Cu_{2-x}S NCs. After that, the color of the methyl viologen changed from colorless to blue color. It was evidence to the tuning ability of LSPR peaks and holes trapping activity.

2.4 Suggested Approaches from Literature

There are two different approaches to address the above mentioned challenges found from literature. The first approach is using the continuous flow regime in a millifluidic device to synthesize different morphologies and compositions of Cu_{2-x}S NCs. The second approach is using the o-phenyldiamine (OPD) compound to develop a dual-model sensing mechanism through the measurement of LSPR absorption and the enhanced fluorescence intensity.

2.4.1 Synthesis of Cu_{2-x}S NCs using Millifluidic Device

It is common and popular to synthesize nanoparticles in bench-top system. Typically, nanoparticles were incubated in round-bottom or flat bottom macro-scale glass flask. The agitation motion was usually involved a magnetic stirrer / sonicator and temperature controller to provide the required thermodynamic energy during the particles synthesis process. However, the macro-scale actuators could produce a relative significant varied temperature difference inside the reaction chamber as shown in Figure 3. There were studies showing that the agitation performance of the sonicator could be varied by the chamber geometry, agitation time, frequency and power [46, 47]. Inconsistent agitation could vary the temperature significantly at different points within the reaction chamber, which altered the precursor re-activities within the system. Different precursors' reactivities could lead the nanoparticles forming different stoichiometric ratios, thereby leading a variety of morphologies and compositions within the same batch.

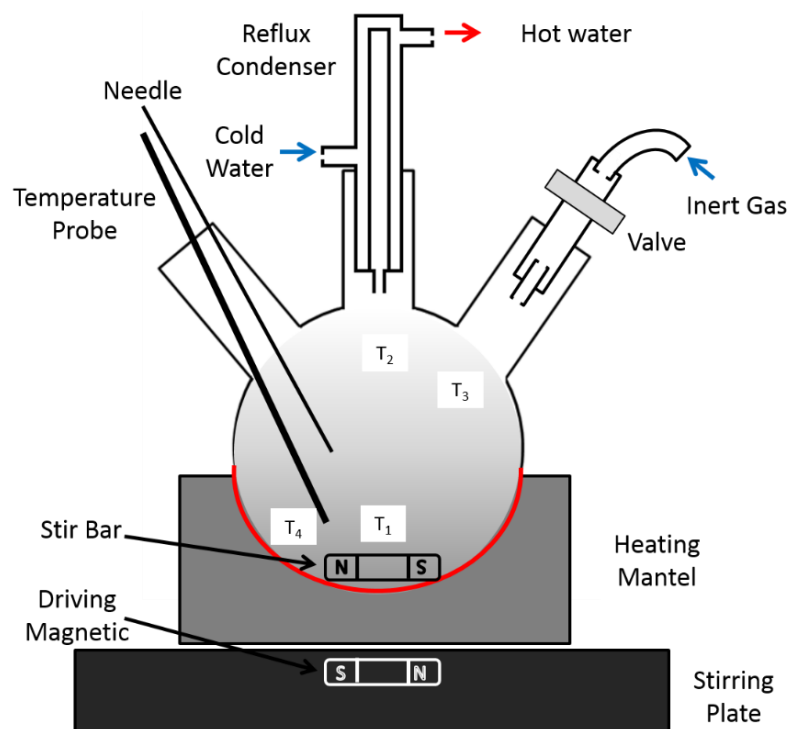


Figure 3 Typical setting up of a bench-top synthesis environment. Various temperature profiles are found due to different inputs from reflux condenser, inert gas, heating mantel and stirring bar etc.

Apart from the batch-top synthetic approach, there were many research works devoted in continuous-flow microfluidic synthesis. This approach allows a precise addition of precursors onto the chip with uniform heating environment [48]. There were many instances for nanoparticles synthesis such as Au [49, 50], CdS [51], Fe₃O₄ [52], and CdSe [53], with achieved size-control synthesis. Continuous-flow synthesis could also alter the compositions and crystal structures of nanoparticles [54], enhanced magnetic intensity [55] and reduced full-width-half-maximum of the fluorescence emission [56]. The simple continuous-flow synthesis was also able to accomplish the complex core-shell CdSe/ZnS [57]. However, microfluidic synthesis approach consisted of many disadvantages including the complicated fabrication procedure, time-consuming, low production rate and high production cost [58-60].

Synthesis in a continuous-flow millifluidic device is another option for nanoparticles fabrication. As shown in Figure 4, synthesis in a millifluidic device not only shared similar advantages with microfluidic such as uniform heating [48, 61], it also consisted of comparative advantages such as simple fabrication, shorter throughput time and suitability for the in-situ operations like X-ray absorption spectroscopy [59]. There were many reports demonstrated that using millifluidic device to synthesize ultra-small Cu nanoclusters, Cu nanoparticles and Fe₂O₃ nanoparticles [60, 62, 63]. There was empirical research indicating that using continuous flow millifluidic synthesis is able to achieve size-control such as of silver and gold nanoparticles [59, 64, 65]. In addition, flow synthesis was capable to achieve size control of nanoparticles. Murphy's group has published a novel size and shape control of gold nanoparticles using continuous-flow millifluidic device as shown in Figure 5 [66]. Tadmouri's et al. demonstrated the morphological control of the nanoparticles using multi-phase mode millifluidic device [67].

Millifluidic on-chip fabrication approach offers an ideal incubation platform for the growth of nanoparticles. For instance, it possessed a large surface area-to-volume geometry, therefore heat can be distributed uniformly during the synthesis [48, 61]. Moreover, the enlarged channel size can increase the production rate as well as the throughput rate, providing an enormous potential for large scale production [68, 69]. Furthermore, nanoparticles synthesized in laminar flow approach could maintain consistent contact between the fluid and thereby kept a consistent stoichiometry ratio between precursors [70].

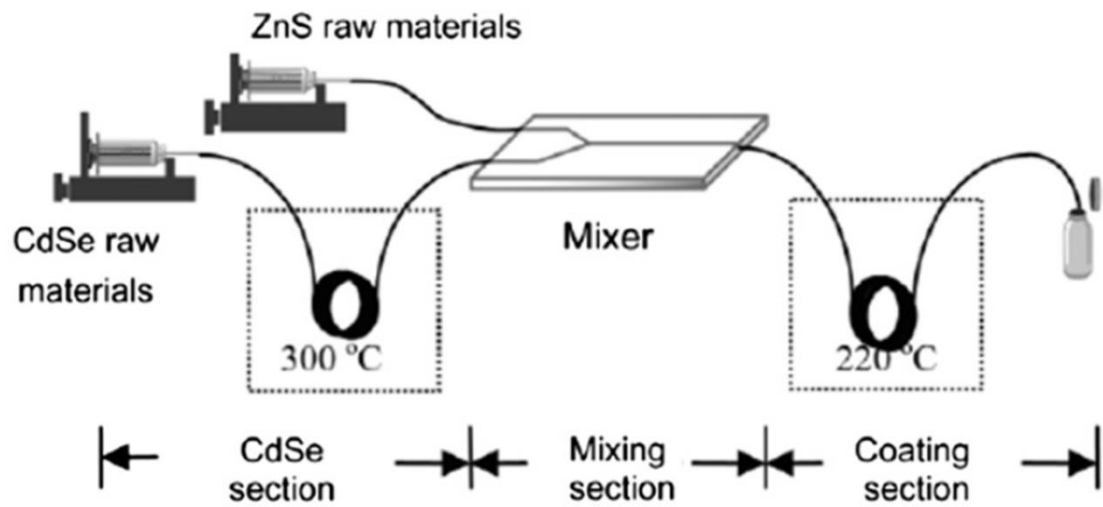


Figure 4 Uniform heating incubation environment from the continuous flow microfluidic channel device demonstrated by Zhao et al. [61]

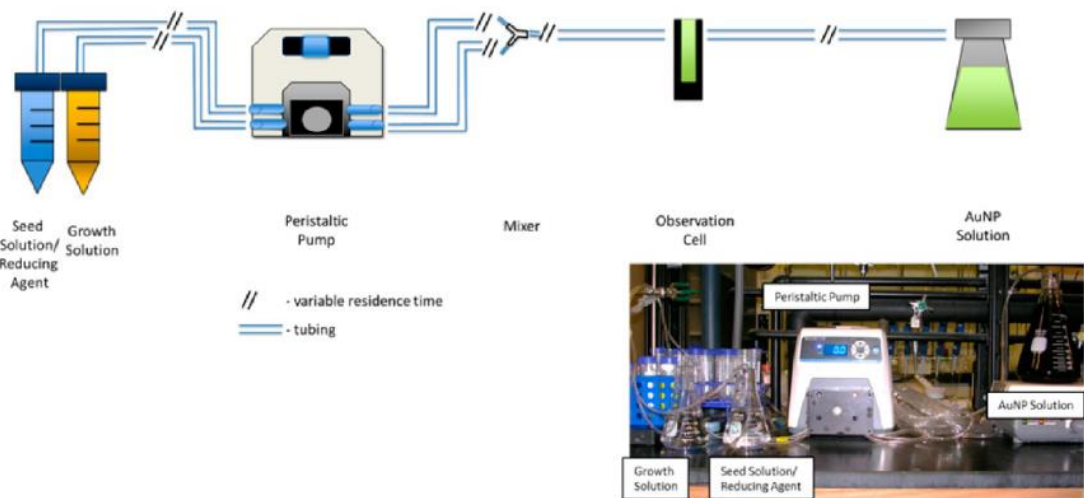


Figure 5 Continuous flow microreactor for AuNP synthesis designed and performed by Catherine J. Murphy et al. [66].

Synthesize nanoparticles by this high continuity and high repeatability device is a promising method for mass production of high quality nanoparticles. This approach is then named as a nanomanufacturing platform. This platform allows definite control of reaction time since the reaction can be stopped desirably through a

particular length of channel. This distance-to-time property enables the size-control of nanoparticles and other fine tuning of nanoparticles for specific needs in sensing and imaging application. Therefore, it was suggested that using millifluidic on-chip fabrication to synthesize the Cu_{2-x}S NCs.

2.4.2 Development of New Sensing Mechanism

After synthesizing a variety of morphologies and compositions of Cu_{2-x}S NCs, the study had moved forward to investigate their plasmonic properties. This study was performed by altering the external refractive index of the solvent and monitored the relative shifting of the LSPR peaks. There were studies shown that the LSPR could be tuned by different shape of nanoparticles. For instances, spherical shape gold nanoparticles had only one LSPR peak at around 520 nm while rod-shaped gold nanoparticles had two peaks. Irregular-shaped nanoparticles such as gold nanobranched even exhibited a better sensitivity than the rod-shaped and spherical gold nanoparticles did [71].

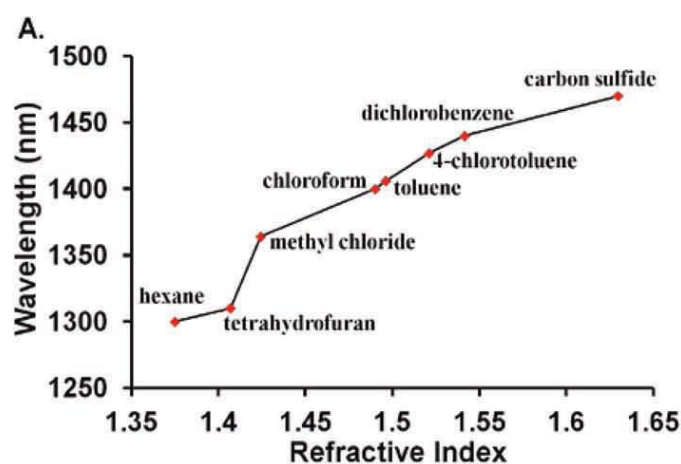


Figure 6 Refractive index dependence plasmonic property of Cu_{2-x}S NCs reported by Liu et al. [6]

LSPR was not only altered by the shape of the nanoparticles, size was another critical factor on the plasmonic property and its sensitivity. As shown in Figure 7, various sized nanoparticles, Cu_{2-x}S NCs, exhibited different plasmonics field which affected the sensitivity of the interacting surface area. There were studies reported that around 40 nm sized spherical gold nanoparticles exhibited the highest sensitivity in a SPR sensor among different sized gold nanoparticles (12 to 80 nm) [72, 73].

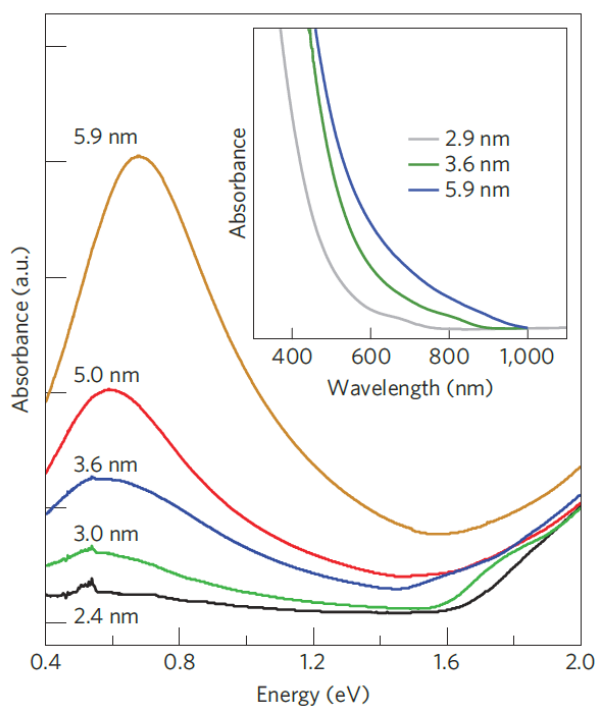


Figure 7 Size dependence plasmonic property of Cu_{2-x}S NCs revealed by Luther et al.

[2]

Chemical composition of the Cu_{2-x}S NCs is another factor to influence the sensitivity of the Cu_{2-x}S NCs as shown in Figure 8. Different compositions of Cu_{2-x}S NCs indicated a variety of crystal structures and the degrees of copper-deficiency. For instance, $\text{Cu}_{1.1}\text{S}$ NC has a higher degree of copper-deficiency (i.e. $x = 0.9$) and belongs to the hexagonal crystal structure, while $\text{Cu}_{1.97}\text{S}$ NC has a lower degree of copper-deficiency (i.e. $x = 0.03$) and belongs to the monoclinic crystal structure. It was suggested that the higher degree of copper-deficiency possessed a higher mobility for the carriers inside the crystal than the lower number of deficiency one [2]. A study showed that the sensitivity of the varied copper sulphide compositions (i.e. Cu_1S , $\text{Cu}_{1.4}\text{S}$ and Cu_2S) exhibited differently. In this study, $\text{Cu}_{1.4}\text{S}$ showed the highest sensitivity due to its non-stoichiometric phase [31]. Since the Cu_{2-x}S NCs were heavily-doped and non-stoichiometric, the number of free holes or carrier density could be varied in terms of chemical compositions, therefore, Cu_{2-x}S NCs could exhibit different localized plasmonic field properties and resulted in different sensitivity to the surrounding.

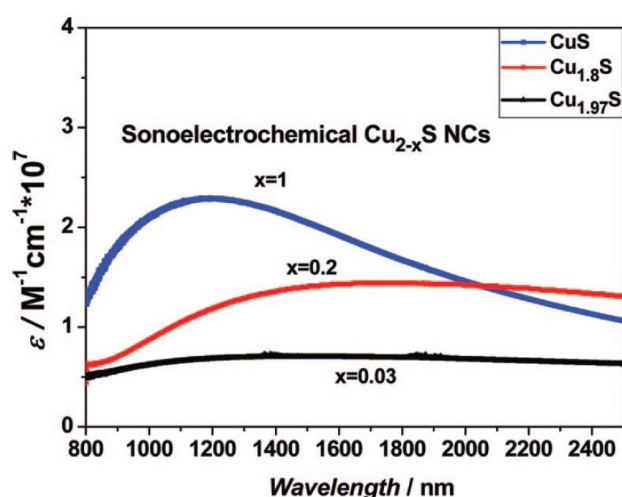


Figure 8 Composition dependence plasmonic property of Cu_{2-x}S NCs demonstrated by Burda et al. [1]

In order to study the effective working range of the new proposed sensing mechanism, different concentrations of the Cu_{2-x}S NCs were investigated. As over-concentrated or too-diluted environment would lead a low signal-to-noise ratio or “waste” of the nanoprobe, it has to decide the optimal concentration and suggested the range of detection.

Apart from the study on the plasmonic properties of different morphologies and compositions of Cu_{2-x}S NCs by altering the external refractive index of a solvent, this study moved forward to cover plasmonic quenching property. Since the LSPR absorption of Cu_{2-x}S NCs could be tuned reversibly through the control of the number of holes in the semiconductor Cu_{2-x}S NCs [3]. This new sensing mechanism could be exploited for the enhancement of the plasmonic sensitivity. Recently, Alam et al. [8] has further examined this new mechanism. They have exploited methyl viologen as an electron donor. Since methyl viologen can be photo-chemically induced, when it introduced to the Cu_{2-x}S NCs, methyl viologen is oxidized and electrons were transferred to the Cu_{2-x}S NCs, the number of holes decreased, proportional with the concentration of methyl viologen. With the decrease in the number of holes, the LSPR absorption also dropped until vanished. This study could be used as a development model for a new sensing mechanism.

Chapter 3 Methodology

3.1 Morphologies and Compositions Control of Cu_{2-x}S NCs by Millifluidic Device

This chapter will be divided into three sections including the millifluidic channel design and fabrication, the synthesis setting and the characterization approach. Section one includes all detail dimensions, geometries of the channel and its fabrication procedures. Section two introduces the synthesis platform using millifluidic device and the synthetic parameters such as the flow rates and the concentration of the precursors. Section three contains the materials used, characterization methods and the corresponding equipment used in the study.

3.1.1 Design and Fabrication of Millifluidic Device

The millifluidic device was firstly fabricated by a domestic 3D printer using Acrylonitrile Butadiene Styrene (ABS) plastic as the printing material, as showing in Figure 9a. The geometry of the millifluidic device was designed as $1.5 \text{ mm} \times 1.5 \text{ mm}$ (width \times height) with a total 545 mm long. The total capacity of the device was around 1227 mm^3 , which was able to handle around 1227 μl fluid at the same time. It was designed that the total incubation time was approximately from 15 s to 490 s as the flow rate of fluidic reached as 5000 microliter per minute ($\mu\text{l}/\text{min}$) to 150 $\mu\text{l}/\text{min}$. The 3D printed mould was then filled up by polydimethylsiloxane (PDMS), as the ultimate millifluidic device.

The actual view of the PDMS millifluidic device has shown in Figure 9b. The PDMS was firstly prepared by the mixture of the resin and the corresponding curing agent (volumetric ratio as 1:10). Then, the as-prepared PDMS was poured into the ABS mould. The PDMS was cured after 4 hours heating at 65°C. After that, the PDMS layer was removed from the ABS mould and placed on a flat 76 mm × 52 mm glass slide. All the inlets were punched by a 4 mm diameter puncher, and connected to the identical length polytetrafluoroethylene (PTFE) tubes. Finally, needles with 1.2 mm diameter were inserted into the other end of PTFE tubes for feeding the precursors and the collection of nanoparticles.

The schematic description and the actual view of nanoparticles fabrication in the millifluidic device are shown in Figure 9c and 1d respectively. From Figure 9d, it is clear that the solution became darker when it flowed along the millifluidic channel. The copper precursor and the sulfur precursor were firstly fed into the device and then mixed in the twisting section. After that, the mixed precursors underwent nucleation in the following straight channel where the copper molecules and sulfur molecules started to aggregate and formulated as a “nuclear” nanocluster. The nucleation stage refers to the light green color of the solution in Figure 9d. Since then, the nuclear was further growing to become a larger sized particle and the color of the solution became darker. Finally, the growth of the nanoparticles were stopped and quenched by the absolute ethanol. The Cu_{2-x}S NCs were collected by mixing with absolute ethanol in 1 to 1 volumetric ratio. The Cu_{2-x}S NCs were separated by centrifugation method (8000 rpm in 2 minutes), and re-dispersed in organic solvents such as chloroform and toluene for different further applications.

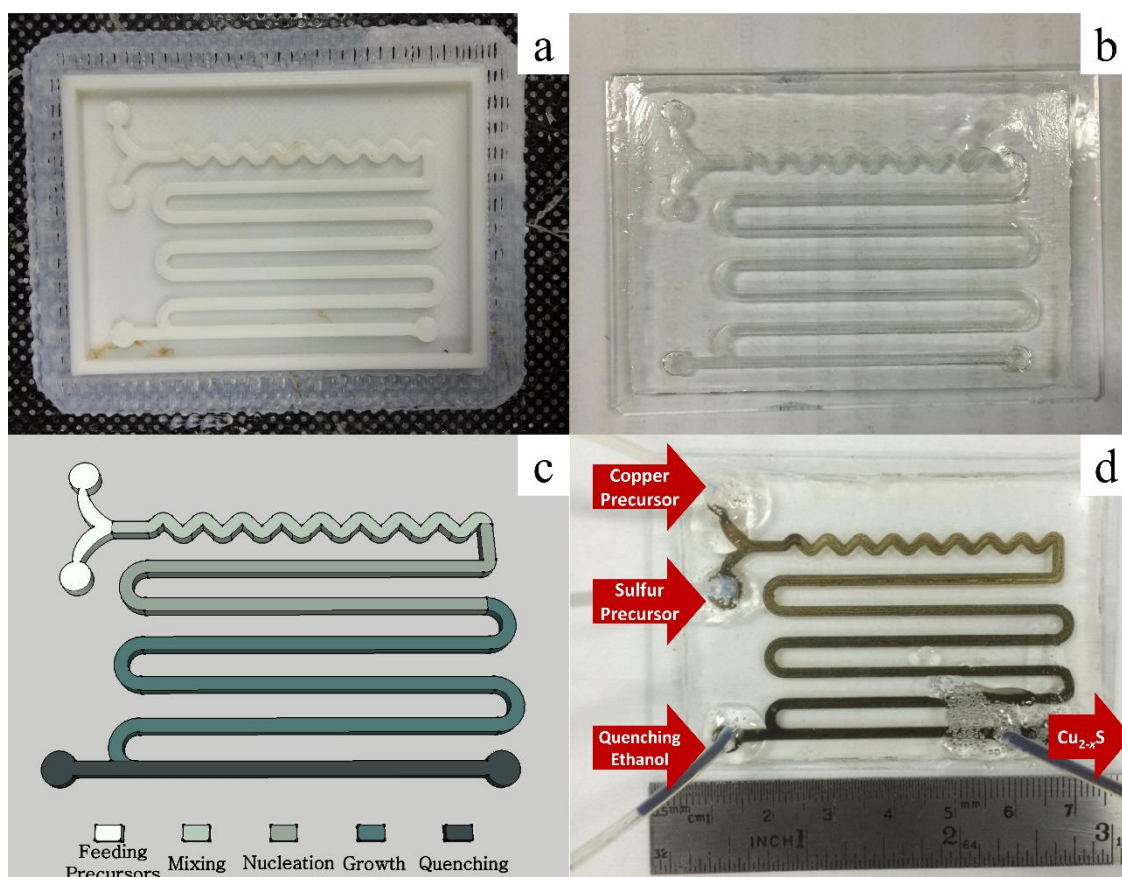


Figure 9 (a) 3D printed ABS mould for the PDMS millifluidic device (b) Top view of the PDMS millifluidic device. (c) Schematic description of nanoparticles fabrication in the continuous-flow millifluidic device (d) Nanoparticles fabrication in PDMS millifluidic device.

This millifluidic device has demonstrated a simple and versatile platform for precise fabrication of nanoparticles. This device could be suitable for synthesizing many kinds of nanoparticles. Since the millifluidic device possesses a large surface area to volume feature which expedite the temperature raised quickly while maintaining a high uniformity heating [48, 61]. This leads to a shorter nucleation time of nanoparticles which is favourable for organic phase synthesis.

Besides, it is important to mention that this millifluidic on-chip fabrication design did not require specific oxygen-free environment during the continuous-flow process. In contrast to the conventional bench-top synthesis system, which the reaction

chamber must be pumped with positive pressure of inert gas such as argon or nitrogen gas, in order to provide the oxygen-free environment. If the oxygen-sealing fails, the precursors might be oxidized and resulting the failure of the synthesis. Another beauty of this simple passive millifluidic device is that it did not require any sophisticated mechanical components and electrical signal inputs, such as micro-electro-mechanical systems[74]. The relative small sized channel also ensured that the laminar flow without turbulence since the Reynolds number is low[75]. The fixed geometry and dimension promised a high reproducibility which is favorable in large-scale fabrication. Lastly, there were fewer reagents used in this continuous-flow synthesis comparing to the bench-top synthesis. Therefore, it could consume less chemical and reduce the environmental impact[61].

3.1.2 Synthetic Setting for Cu_{2-x}S NCs Fabrication

In order to fabricate different compositions and morphologies of Cu_{2-x}S NCs, we have deployed two different synthetic settings for it. The first setting is to vary the precursors' concentration and the second setting is to vary the flow rates of the precursors.

Before implementing those settings, the precursors were prepared in advance referring to the previous report [6]. In detail, the sulfur powder with different amounts (10 mmol, 6 mmol and 1 mmol) were mixed with 10 ml oleic acid (OA) in a round bottom three-neck flask by vigorous stirring. The flask was pumped with nitrogen gas and heated at around 120 °C for degassing at around 30 minutes. On the other hand, the copper (I) chloride with different amounts (10 mmol, 6 mmol and 1 mmol) were mixed with 10 ml oleylamine (OAm) in a round bottom three-neck flask by vigorous stirring. The flask was also pumped with nitrogen gas and heated at around 120 °C for degassing at around half an hour. After that, the copper-oleylamine (OAm-Cu) mixture became greenish yellow color, then it was further heated up to 200 °C until it became a colorless or slightly yellowish color, which indicated a fully reduced state. The mixture was then cooled down to 120 °C and withdrawn by a syringe for the next-step on-chip fabrication. Similarly, the colorless or slightly yellowish color sulfur-oleic acid (OA-S) precursor was withdrawn by a glass-made syringe.

Before feeding the precursors into the microfluidic device, the microfluidic device was placed on a 120 °C hot plate before the fabrication. The two precursors were connected to the PTFE tubes and placed on a microliter syringe pump. Once the pump actuated, the precursors were fed into the channel and then the Cu_{2-x}S NCs

started to grow. The growth of the Cu_{2-x}S NCs was quickly terminated by injecting the absolute ethanol at the last row of the channel. Finally, the nanocrystals were separated by centrifugation at 8000 rpm for 2 minutes. Cu_{2-x}S NCs was re-dispersed in chloroform and toluene for different applications.

In order to investigate the morphologies of the Cu_{2-x}S NCs, the precursors were flowed at different rates including 150 $\mu\text{l}/\text{min}$, 1000 $\mu\text{l}/\text{min}$, 2000 $\mu\text{l}/\text{min}$, 3000 $\mu\text{l}/\text{min}$, 4000 $\mu\text{l}/\text{min}$ and 5000 $\mu\text{l}/\text{min}$, while keeping the copper to sulfur molar ratios as 1 to 2. On the other hand, in order to study the compositions or crystal structures of Cu_{2-x}S NCs, the precursors were prepared at varied copper to sulfur molar ratios which are 1:10, 1:6, 1:2, 2:1, 6:1 and 10:1, and maintaining the flow rate at 3000 $\mu\text{l}/\text{min}$.

3.1.3 Material and Characterization Method

For fabrication of Cu_{2-x}S NCs: Copper (I) chloride (99.995%) and sulfur powder (analytical grade) were purchased from Sigma Aldrich Ltd. Organic solvents such as Oleylamine (>50.0%), oleic acid (>85.0%) and toluene (>99.5%) were purchased from Tokyo Chemical Industry Co., Ltd.). Chloroform (ACS standard) and absolute ethanol ($\geq 99.5\%$) were purchased from Merck Pte Ltd). For fabrication of millifluidic device: The 184 Sylgard silicone elastomer kit containing the polydimethylsiloxane (PDMS) base and curing agent were purchased from Dow Corning. Other chemicals: L-Glutathione reduced ($\geq 98.0\%$) was purchased from Sigma Aldrich. Glycerol (86 - 88 %), Sodium hydroxide (98.5 %), o-Phenylenediamine (98 %) and DI water were purchased from Acros Organics. All chemicals were used without any further purification.

All of the as-prepared Cu_{2-x}S NCs were characterized using scanning transmission electron microscopy (STEM), powdered X-ray diffraction (XRD), Energy-dispersive X-ray spectroscopy (EDX), ultraviolet-visible-infrared spectroscopy (UV-Vis-NIR), fluorospectrometer and inductively coupled plasma - optical emission spectrometry (ICP-OES). The characterization data were used to determine the monodispersity, morphology, LSPR peak, fluorescence intensity and the concentration of the as-synthesized Cu_{2-x}S NCs.

3.2 A Study on the Plasmonic Properties of a variety of Morphologies and Compositions of Cu_{2-x}S NCs

After synthesizing a variety of morphologies and compositions of Cu_{2-x}S NCs, their plasmonic properties were investigated. The study was performed by altering the external refractive index environment and monitoring the amplitude of shift of the LSPR peaks. The study on the plasmonic property of different morphology and compositions of Cu_{2-x}S NCs was done in both organic and aqueous phases. For the organic phase, the Cu_{2-x}S NCs were dispersed into five different organic solvents which have different refractive indexes. After that, the organic phase Cu_{2-x}S NCs underwent the ligand exchange process, which enables the hydrophilic of Cu_{2-x}S NCs. The aqueous phase Cu_{2-x}S NCs were dispersed into a series of glycerin-water mixture, which provided a variety of refractive index from 1.333 to 1.3685. The initial concentration and yield of all kinds of Cu_{2-x}S NCs were determined by the inductively coupled plasma optical emission spectrometry (ICP-OES), in order to ensure the common LSPR intensity and positions before the study. This process has been repeatedly deployed in the series of morphologies and compositions of Cu_{2-x}S NCs for the study of its plasmonic property.

3.2.1 Organic Solvent

Cu_{2-x}S NCs were firstly dispersed into five type organic solvents with different refractive index including the hexane (RI = 1.375), dichloromethane (RI = 1.420), chloroform (RI = 1.445), toluene (RI = 1.495) and dichlorobenzene (RI = 1.545). It was expected that as the refractive index medium is increased, the red-shift of the LSPR peaks would be obtained. All the samples contained 65 ppm Cu_{2-x}S NCs and measured by the UV-Vis-NIR spectrometer. Calibration curves of different sizes, shapes and compositions of Cu_{2-x}S NCs were recorded and analyzed.

3.2.2 Aqueous Environment

Since most of the analyte were dispersed in aqueous phase, the study on the plasmonic property in aqueous environment is necessary. Before the study, the Cu_{2-x}S NCs underwent the ligand exchange process by glutathione (GSH) according to the published protocol [76]. It was suggested to employ the high refractive index (RI = 1.475) glycerin to alter the external RI medium. The water-soluble and colorless glycerin was mixed with water (RI = 1.333) by different weight ratios (i.e. 0%, 1%, 5%, 10%, 15%, 25%) which provided a range of refractive index from 1.3330 to 1.3685. The baseline of the study was performed by dispersing the Cu_{2-x}S NCs into DI water. All the samples contained 65 ppm Cu_{2-x}S NCs and recorded by the UV-Vis-NIR spectrometer. Calibration curves of different sizes, shapes and compositions of Cu_{2-x}S NCs were recorded and analyzed.

3.3 A Study on the Plasmonic Quenching and the Fluorescence Enhancement for the Sensing Mechanism Development

Nanoparticles were used as a sensing probe for different kinds of analyte. Typically, metallic nanoparticles exploited its rich carrier density (typically 10^{23} cm^{-3}) to serve as a sensitive probe. This study has employed the semiconductor Cu_{2-x}S NCs and studied its potential sensing ability. Since the plasmonic property of the Cu_{2-x}S NCs is governed by the number of free holes or carrier density, any changes of the free holes would result in LSPR shifting, dropping or vanishing. This property enables the sensing on the redox reaction which consists of electrons transferring and holes trapping activities. As Alivisatos et al. has further suggested that using Cu_{2-x}S NCs as a sensing probe for the redox reaction monitoring [77], our study was based on this inspiring work and employed the o-phenyldiamine (OPD) to study the plasmonic quenching effect on the Cu_{2-x}S NCs. Since OPD has redox property, the electron receptor Cu_{2-x}S NCs would oxidize the OPD through the electron transfer activity. When the heavily doped Cu_{2-x}S NCs met the OPD, it was expected that the electrons would transfer from OPD to the Cu_{2-x}S NCs and trapped holes of Cu_{2-x}S NCs, resulting the plasmonic quenching effect. For the future development in sensing application, OPD compound can be used as a potential labeler by attaching its amine group and the carboxyl group using cross-linker such as EDC and NHS. In addition, some studies have already applied the OPD as a labeler to sense different analyte [35, 78-80] by the cross-linking method. Furthermore, since the oxidized compound OPD (OPD_{ox}) could emit fluorescence light at around 568 nm, therefore the enhanced fluorescence intensity was a reflection of the level of the oxidation of OPD. Therefore, the enhanced fluorescence of different morphologies and compositions of

Cu_{2-x}S NCs were recorded and measured, which could indicate the relationship between the sensitivity of Cu_{2-x}S NCs. The schematic model of the plasmonic quenching and fluorescence enhancement is shown in Figure 10.

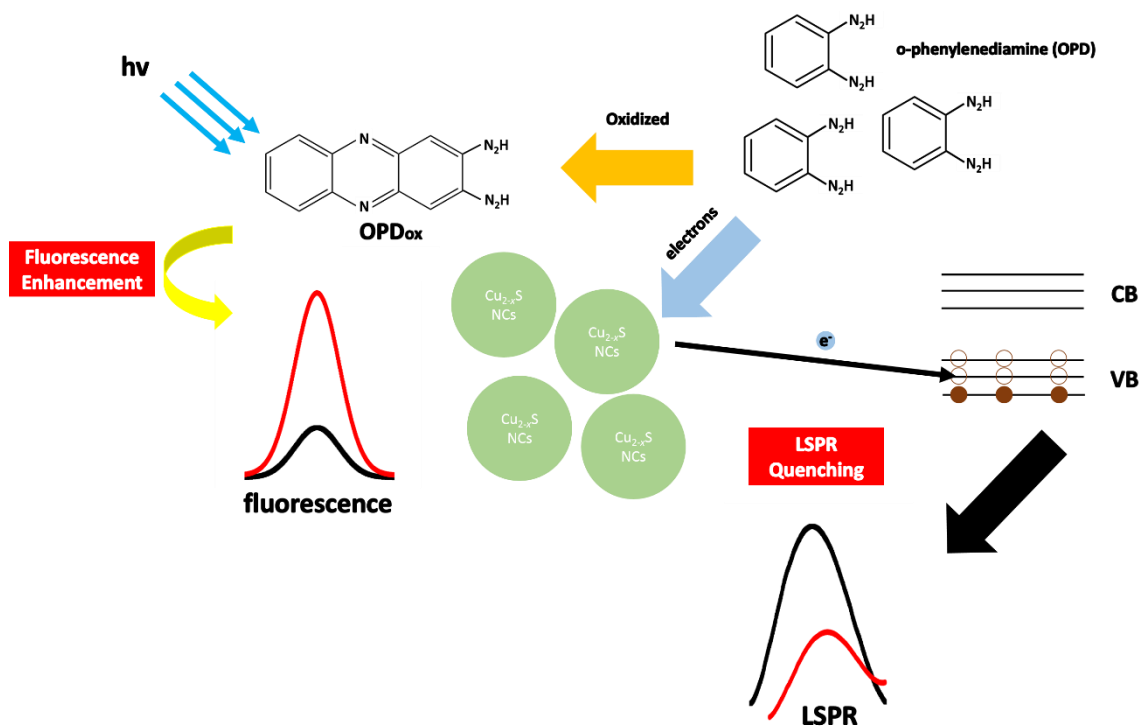


Figure 10 Schematic diagram on the plasmonic quenching and the fluorescence enhancement by the use of o-phenylenediamine (OPD) to the Cu_{2-x}S NCs.

Before the measurement, as the oxygen molecules in the atmosphere might also induced the oxidation of the OPD, in order to eliminate this background noise and provide the accurate result, the first step is to identify the baseline of the fluorescence intensity of OPD in water. The fluorescence intensity of different concentration of the OPD in water (i.e. 1 μM , 10 μM , 100 μM , 200 μM , 2 mM, 20 mM and 200 mM) were measured as shown in Figure 11. The measurement was conducted by exciting with a 390 nm light source and the consistent 568 nm emission was recorded for different amount of OPD. The highest intensity was recorded at around 2×10^4 for 200 mM OPD. This measurement was used as the baseline for the analysis of the fluorescence measurement.

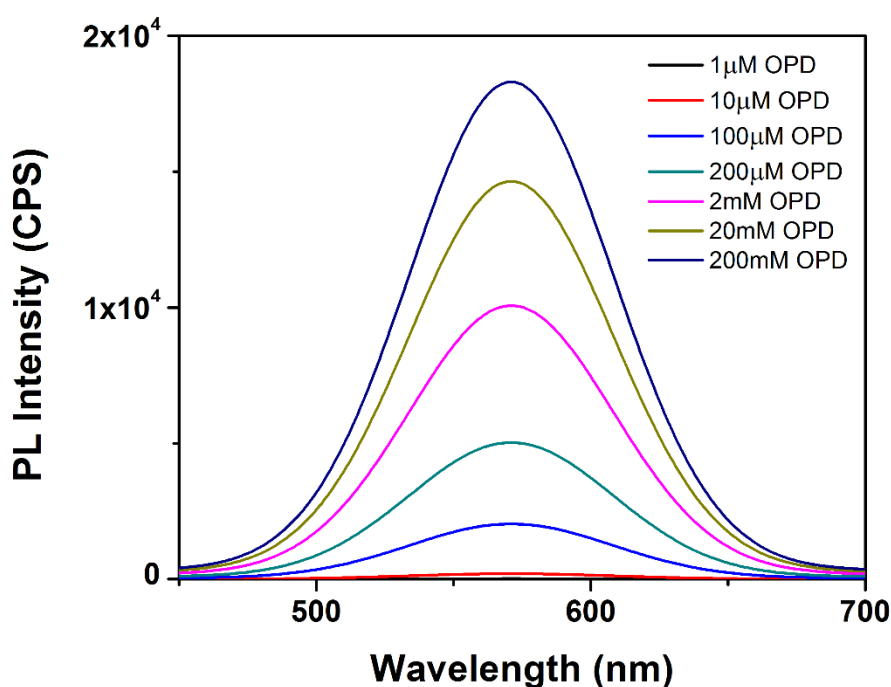


Figure 11 Fluorescence intensity of various concentrations of oxidized o-phenylenediamine (OPDox) in pure water.

Chapter 4 Results and Discussion

This chapter consists of three different sections. The first section focuses on the characterization of the as-synthesized Cu_{2-x}S NCs by the millifluidic device. The second section mentions the plasmonic property in a variety of morphology and compositions of Cu_{2-x}S NCs. The last section discusses on the plasmonic quenching effect and the fluorescence enhancement by different ratios of Cu_{2-x}S NCs and OPD in a variety of morphologies and compositions of Cu_{2-x}S NCs.

4.1 Characterization of the Cu_{2-x}S NCs Fabricated by Millifluidic Device

4.1.1 Morphology Modification

The size and shape control of the Cu_{2-x}S NCs were accomplished by varying the flow rates of the input precursors. As shown in Figure 12, different morphologies of Cu_{2-x}S NCs were synthesized by varying the flow rates and precursors' concentration using the millifluidic device. Table 1 has summarized the results on the detailed dimensions, throughput rate and the production yield by different synthetic parameters. For each batch, there was at least 200 Cu_{2-x}S NCs selected to determine its size, shape and the aspect ratio. The size distributions and the corresponding aspect ratios of these batches are presented in histogram format as shown in Figure 13. By varying the flow rates of precursors from 1000 to 3000 $\mu\text{l}/\text{min}$, rod-shaped with aspect ratio 1.3 to 3.4 Cu_{2-x}S NCs were fabricated. With the increased of the flow rates up to 4000 to 5000 $\mu\text{l}/\text{min}$, spherical Cu_{2-x}S NCs with diameters from 3.6 nm to 8.8 nm were synthesized. It is believed that the growth mechanism of the rod-shaped Cu_{2-x}S NCs was a prolonged nucleation due to variation of the flow rates. When the molecular size precursors reacted in the small millifluidic channel under a

high flowing speed, it might not have sufficient time to form adequate nuclei for Cu_{2-x}S NCs. This unique incubation environment could allow more molecular size precursors reacted on the relative active facet of the nuclei, and resulting the rod-shaped Cu_{2-x}S NCs. Similar finding was also reported by Choi et al. In their study, rod-shaped nanoparticles were fabricated according to this growth mechanism. It was suggested that the variation of the morphology might be attributed to the binding between the precursors and the reactive facet of the nuclei during the seed-mediated growth process [81]. When the flow rates further raised to 4000 $\mu\text{l}/\text{min}$ and 5000 $\mu\text{l}/\text{min}$, spherical Cu_{2-x}S NCs with diameters of 8.8 nm and 3.6 nm were produced. This finding was aligned with the previous suggested growth mechanism. Since these high fluidic speeds (i.e. 4000 $\mu\text{l}/\text{min}$ and 5000 $\mu\text{l}/\text{min}$) had further reduced the incubation time of the Cu_{2-x}S NCs (i.e. less throughput time), so that less molecular size precursor underwent less reaction time and thereby resulted in the smaller size nanoparticles and spherical shaped.

On the other hand, it was shown that the alteration of the molar ratio between the precursors lead to slight morphological change of Cu_{2-x}S NCs. Similarly, for each batch, there was at least 200 Cu_{2-x}S NCs selected to determine the size, shape and the aspect ratio. The size distributions and the corresponding aspect ratios of the batches are presented in histogram format as shown in Figure 14. As the molar ratio between the oleic acid-sulfur precursor (OA-S) and the oleylamine-copper (OAm-Cu) precursor reached 1:10, some spherical particles were observed. As the molar ratios further reduced to 1:6 and 1:2, rod-shaped Cu_{2-x}S NCs with aspect ratio of 2.3 and 3.4 were synthesized respectively. When the molar ratio of the OA-S and OAm-Cu further reduced to 2:1, 6:1 and 10:1, the copper-rich reactants formulated the spherical Cu_{2-x}S NCs with diameters of 8.8 nm, 11.9 nm and 12.6 nm respectively.

The small scale morphological change might be due to the variation of the molar ratio that affects the binding activities of the nuclei.

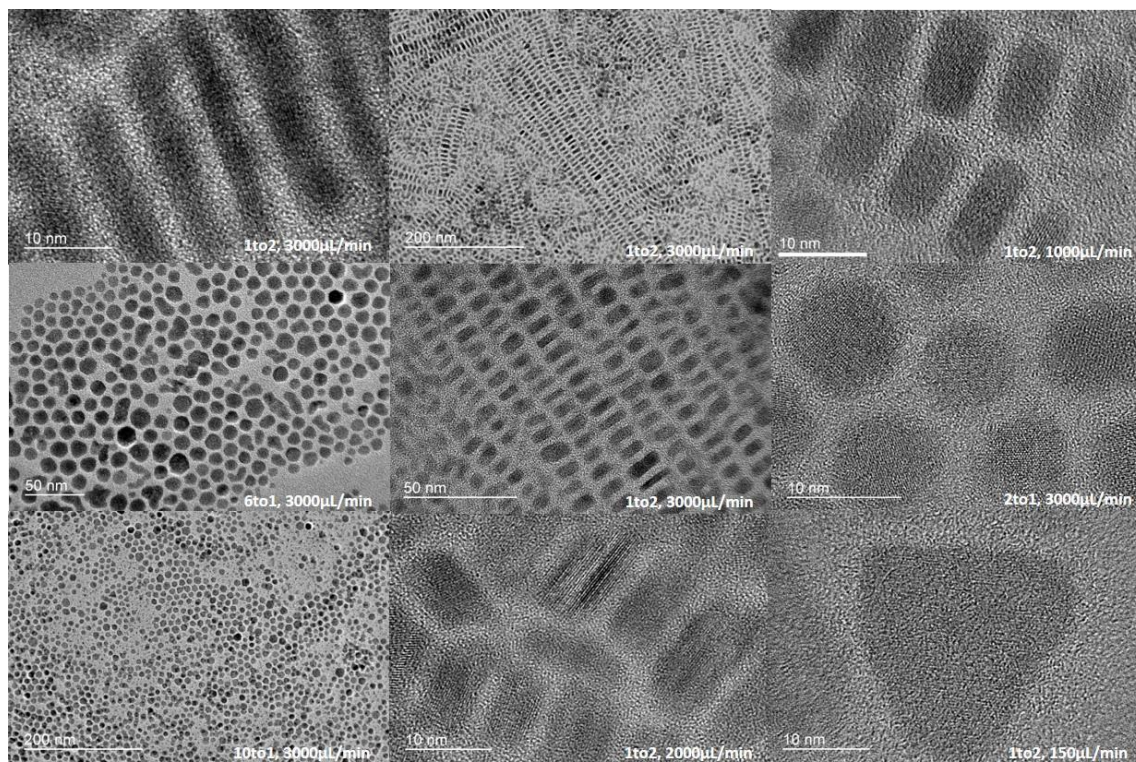


Figure 12 TEM images for different morphologies of Cu_{2-x}S NCs. Distinct morphologies of Cu_{2-x}S NCs were modified by varying the flow rates and precursor concentration in the millifluidic device.

Table 1 Summary of the morphologies, compositions and plasmonic absorption peaks of Cu_{2-x}S NCs by varying different flow rates and the copper to sulfur molar ratios

Molar Ratio (Cu:S)	Flow Rate ($\mu\text{l}/\text{min}$)	Shape	Dimension D: Diameter (nm) L: Length (nm) W: Width (nm)	Aspect Ratio	Throughput Time (s)	¹ Yield (%)	Structure	LSPR Peak (nm)
1:10	3000	Spherical	D: 6.4	1.2	25	86	Covellite	1115
1:6	3000	Rod	L: 12.0, W:	2.3	25	87	Covellite	1150
1:2	3000	Rod	5.3	3.4	25	90	Covellite	1272
2:1	3000	Spherical	L: 13.9, W:	1.1	25	93	Roxbyite	1315
6:1	3000	Spherical	4.3	1.1	25	94	Djurleite	1471
10:1	3000	Spherical	D: 8.8	1.1	25	97	Djurleite	1641
1:2	1000	Rod	D: 11.9	1.3	72	91	Covellite	1246
1:2	2000	Rod	D: 12.6	2.3	37	87	Covellite	1266
1:2	4000	Spherical	L: 7.8, W: 6.2	1.1	18	78	Spionkopite	1293
1:2	5000	Spherical	L: 12.0, W: 5.3 D: 8.8 D: 3.6	1.2	15	67	Spionkopite	1277

¹Yield (%): It refers the ratio between the number of Cu_{2-x}S NCs synthesized and the initiated number of moles inputted. The number of Cu_{2-x}S NCs synthesized was measured by ICP-OES and the initiated number of moles inputted referred to the molar ratio (Cu:S) in column 1.

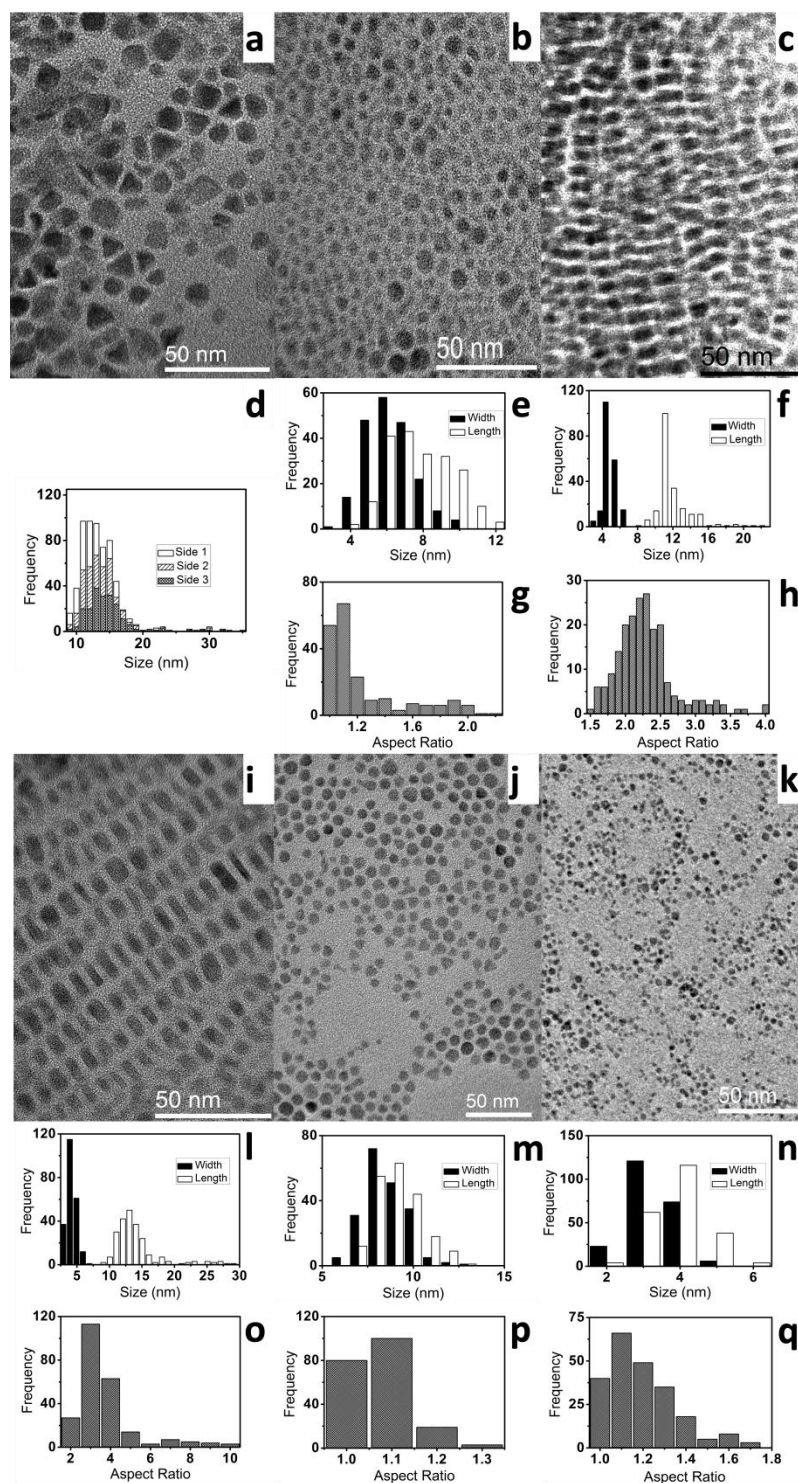


Figure 13 TEM images of Cu_{2-x}S NCs exhibiting different morphologies synthesized at flow rates of (a) 150 $\mu\text{l min}^{-1}$, (b) 1000 $\mu\text{l min}^{-1}$, (c) 2000 $\mu\text{l min}^{-1}$, (i) 3000 $\mu\text{l min}^{-1}$, (j) 4000 $\mu\text{l min}^{-1}$ and (k) 5000 $\mu\text{l min}^{-1}$, and their respective size distributions (d, e, f, l, m and n) and aspect ratios (g, h, o, p and q). The precursors' concentration between Cu : S kept at 1 : 2.

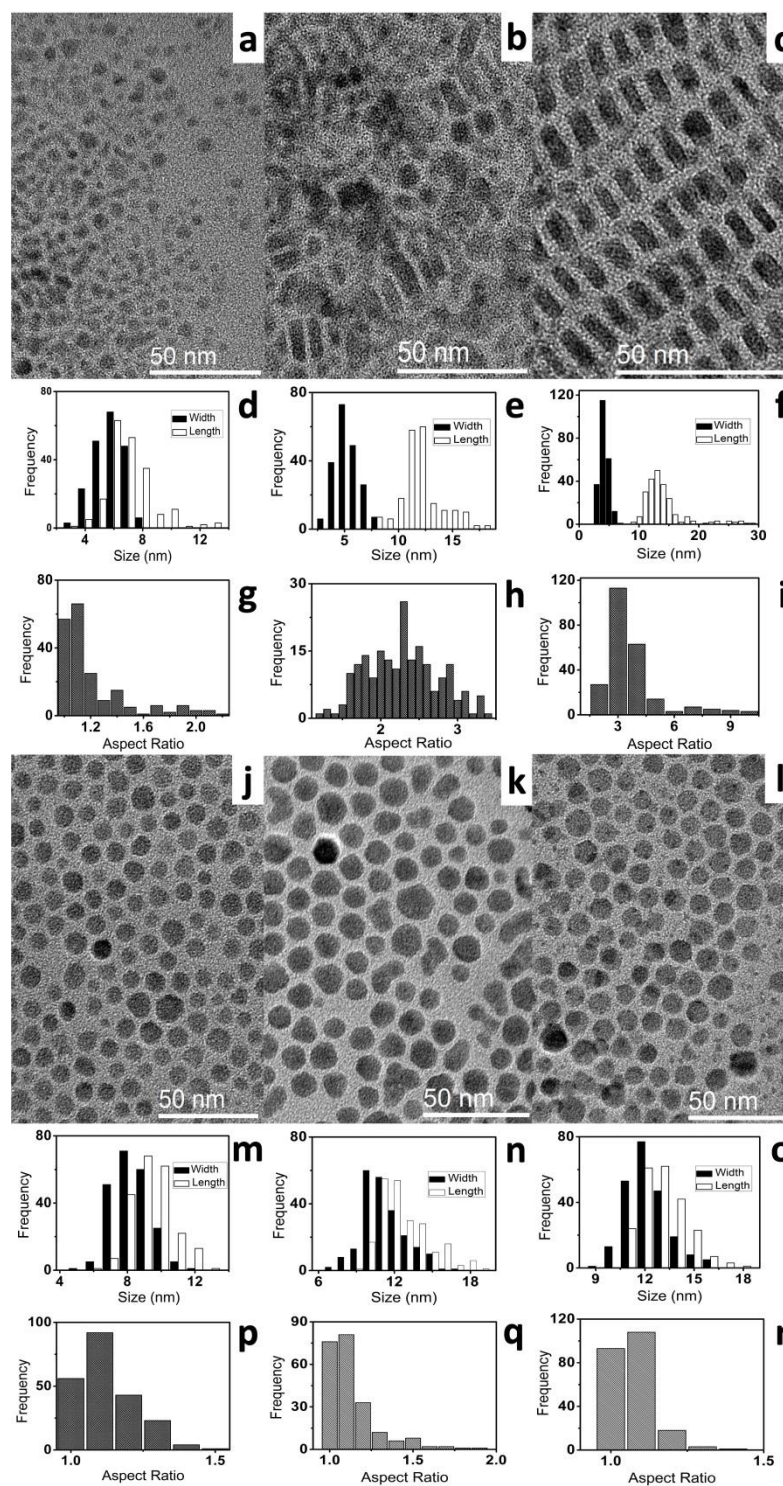


Figure 14 TEM images of Cu_{2-x}S NCs synthesizing at different precursors' concentration of $\text{Cu} : \text{S}$ for (a) 1 : 10, (b) 1 : 6, (c) 1 : 2, (j) 2 : 1, (k) 6 : 1 and (l) 10 : 1, exhibiting different morphologies and their respective size distributions (d, e, f, m, n and o) and aspect ratios (g, h, i, p, q and r). The flow rate was set at $3000 \mu\text{l min}^{-1}$.

4.1.2 Composition Modification

The composition modification of the Cu_{2-x}S NCs was accomplished mainly by the variation of the precursors' concentration. As the molar ratios are altered from 1:10, 1:6 and 1:2, Cu_{2-x}S NCs were formed with the covellite ($\text{Cu}_{1.1}\text{S}$) structure. As shown in Figure 15a, the diffraction peaks of the XRD patterns were found at 29.25° , 31.76° , 32.82° and 47.89° , which the corresponding is (102), (103), (006) and (110) planes of covellite structure. Furthermore, the nanocrystals were also characterized by the high resolution transmission electron microscopy (HRTEM) as shown in Figure 17. In Figure 17a and c, it shows that the lattice distance of the nanocrystals were 2.815 \AA and 1.898 \AA which corresponds to the (1 0 3) and (1 1 0) crystallographic planes of the hexagonal covellite (as PDF card number 01-078-2391). The following FFT analysis shown in Figure 17b and d also reinforce the statement of the covellite structure.

When the molar ratio between the copper and sulfur precursors increased, the XRD patterns shown in Figure 15b exhibits major peaks at 26.59° , 31.20° , 34.06° , 46.84° and 48.90° , which points out to the respective (16 0 0), (18 2 1), (20 0 1), (0 16 0) and (886) planes of roxbyite structure. Further to the characterization by the high resolution transmission electron microscopy (HRTEM) in Figure 17i, it shows that the lattice distance of the nanocrystal is 1.938 \AA which refers to the (0 16 0) crystallographic plane of the monoclinic roxbyite (as PDF card number 00-023-0958). The following FFT analysis shown in Figure 17j of the particle also reveals the same roxbyite structure.

With the molar ratios increased to the copper-rich setting as 6:1 and 10:1, the copper-rich djurleite ($\text{Cu}_{1.97}\text{S}$) was formed. The major diffraction peaks in the XRD

patterns shown in Figure 15c were found at 26.27° , 37.62° , 46.13° , 46.31° and 48.65° , referring to the respective (004), (804), (046), (080) and (12 0 4) planes of djurleite structure. Moreover, the HRTEM images shown in Figure 17e and g also reveal that the lattice patterns of the nanocrystals are 1.870 \AA and 2.389 \AA respectively. The lattice patterns refer to the (12 0 4) and (8 0 4) crystallographic planes of the monoclinic djurleite as suggested by PDF card number 00-023-0959). Figure 17f and h also presents the FFT analysis for the individual particles and it further confirms the djurleite structure of the nanocrystals.

Furthermore, the XRD patterns were also analyzed by the rietveld refinement analysis. From Figure 18, the experimental XRD data were only moderately fitted to the corresponding PDF Card data despite resemble decent general trend was found. This might be due to the nature of the collected data from the prepared samples (e.g. thickness of sample deposited on the substrate, concentration of the samples, mixed phases of nanocrystals, etc). To further probe the nanocrystals properties, EDX measurements were deployed by drop-casting method. The results were mentioned in Table 2, it has revealed that multiple phases of Cu_{2-x}S NCs were existed in the samples especially for those with higher copper compositions. In Figure 19 below corroborates this discussion as there were significantly larger standard deviations of the copper in both cases of the 6:1 and 10:1 copper is to sulfur molar ratios. Therefore, it was generally believed that the obtained Cu_{2-x}S NCs were multi-phased and thereby resulting the varied XRD patterns from the PDF Card database one.

Variation on the flow rates could only able to alter the compositions from covellite ($\text{Cu}_{1.1}\text{S}$) to spionkopite ($\text{Cu}_{1.39}\text{S}$). The XRD patterns shown in Figure 16a have revealed that the compositions of the Cu_{2-x}S NCs fabricated under the flow rates of

1000 to 3000 $\mu\text{l}/\text{min}$. The diffraction peaks were exhibited at 29.25° , 31.76° , 32.82° and 47.89° , the correspond to (102), (103), (006) and (110) planes of covellite structure. As the Cu_{2-x}S NCs fabricated under a higher flow rates as 4000 and 5000 $\mu\text{l}/\text{min}$, the diffraction peaks shown in Figure 16b were found at 29.00° , 32.21° , 47.57° and 50.08° corresponding to (605), (608), (660) and (6 0 19) planes of spionkopite structure. Similarly in Figure 17k, the lattice distance of 1.910 \AA refers to the (6 6 0) crystallographic plane of the hexagonal spionkopite as suggested by the PDF card number 00-036-0380). The spionkopite structure was further reinforced by the FFT analysis as depicted in Figure 17l.

The Cu_{2-x}S NCs exhibited a negligible morphological change but significant modification in the composition. In general bench-top incubator, Cu_{2-x}S NCs is usually fabricated as covellite ($\text{Cu}_{1.1}\text{S}$), anilite ($\text{Cu}_{1.75}\text{S}$), digenite ($\text{Cu}_{1.8}\text{S}$), djurleite ($\text{Cu}_{1.95}\text{S}$) and the stoichiometric chalcocite (Cu_2S) under the atmospheric pressure and temperature [82]. On the other hand, our millifluidic device possesses a distinct pressure environment due to its relative small enclosed geometry. This specific incubation environment might assist the formation of the unusual roxbyite ($\text{Cu}_{1.75}\text{S}$) and spionkopite ($\text{Cu}_{1.39}\text{S}$).

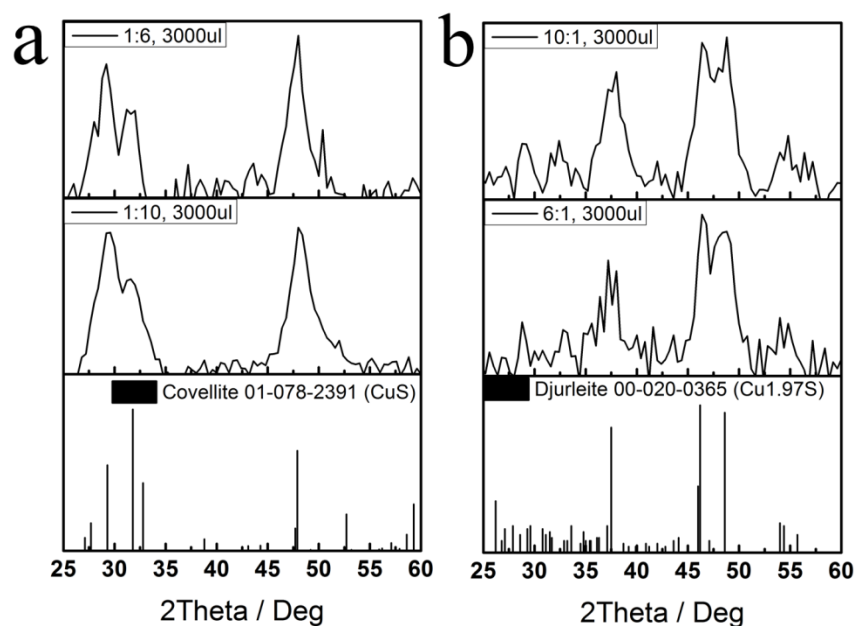


Figure 15 XRD patterns for the modification of the compositions of Cu_{2-x}S NCs by varying precursors' concentrations. a) covellite $\text{Cu}_{1.1}\text{S}$ (PDF Card 01-078-2391) b) roxbyite $\text{Cu}_{1.75}\text{S}$ (PDF Card 00-0232-0958) and djurleite $\text{Cu}_{1.97}\text{S}$ (PDF Card 00-020-0365)

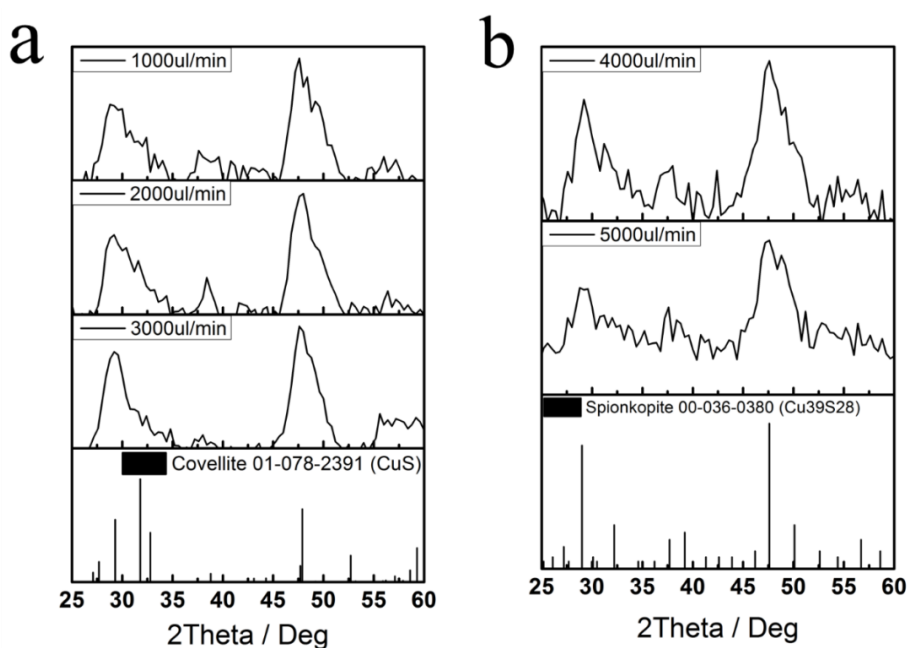


Figure 16 XRD patterns for the modification of the compositions of Cu_{2-x}S NCs by varying the flow rates of the precursors. a) covellite $\text{Cu}_{1.1}\text{S}$ (PDF Card 01-078-2391) and b) spionkopite $\text{Cu}_{1.39}\text{S}$ (PDF Card 00-036-0380)

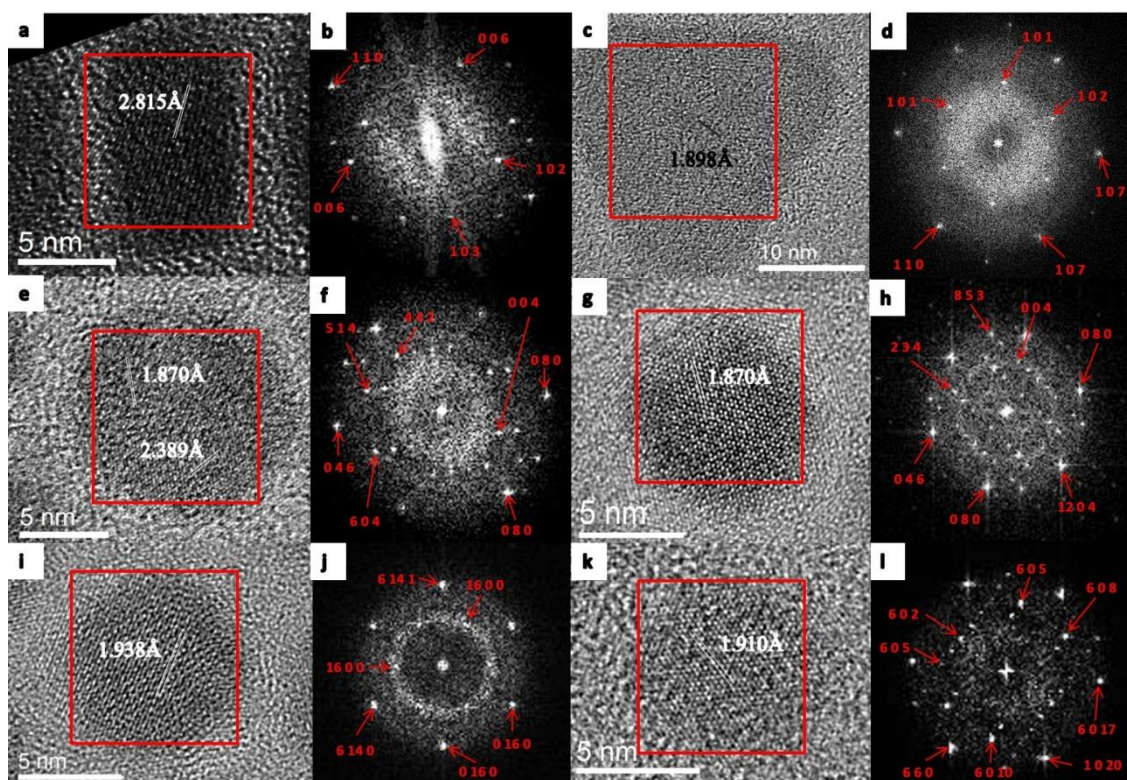


Figure 17 HRTEM images of individual nanoparticle with different compositions of covellite (a and c), djurleite (e and g), roxbyite (i) and spionkopite (k), and the corresponding FFT analysis for covellite (b and d), djurleite (f and h), roxbyite (j) and spionkopite (l).

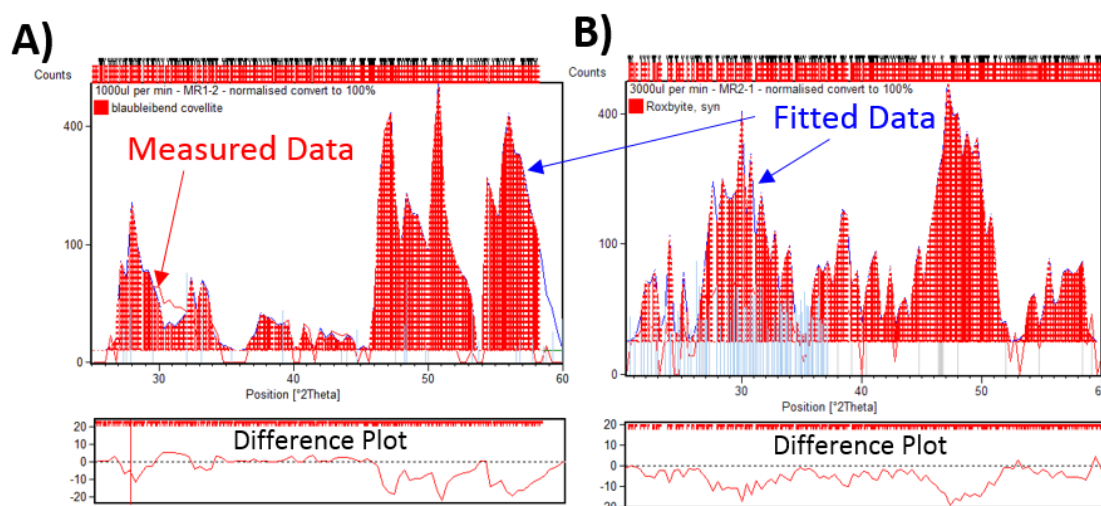


Figure 18 Rietveld refinement XRD fitting for different Cu_{2-x}S NCs sample data – A) 1:2 (Cu:S) molar ratio with 1000 $\mu\text{l}/\text{min}$ flow rate B) 2:1 (Cu:S) molar ratio with 3000 $\mu\text{l}/\text{min}$. Blue curve shows the fitted Rietveld refinement profiles and the red curve shows the measured data. The corresponding difference plots between the fitted data and the measured data are also included respectively.

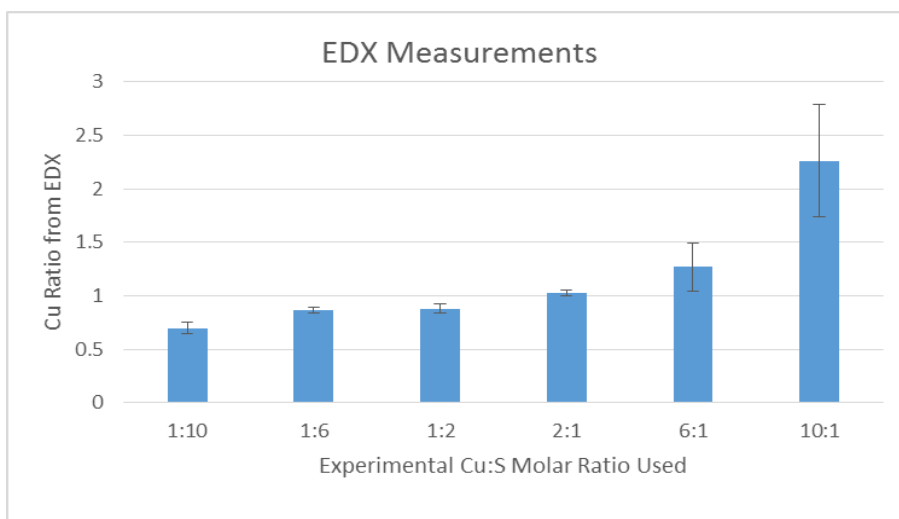


Figure 19 EDX measurements for Cu_{2-x}S NCs using different precursor's concentration.

Table 2 EDX composition ratios compared against the XRD fittings

Cu:S Molar Ratio	EDX Composition Ratio	
	Cu	S
10:1	2.26±0.53	1
6:1	1.27±0.22	1
2:1	1.02±0.03	1
1:2	0.88±0.04	1
1:6	0.86±0.03	1
1:10	0.70±0.05	1

4.1.3 LSPR Spectra of the Cu_{2-x}S NCs by Varying Different Flow Rates and Precursors' Concentration

As the localized surface plasmonic resonance (LSPR) absorption in the near infrared (NIR) region was contributed to the free holes of the heavily-doped semiconductor Cu_{2-x}S NCs, different number of free holes (different x -value) of Cu_{2-x}S NCs could express a variety of LSPR profile in the NIR region. As shown in Figure 20, the LSPR peaks were varied from 1246 nm to 1293 nm and 1115 nm to 1644 nm, by varying the input flow rates and the molar ratio between the precursors respectively. It was observed that a relative small magnitude of the LSPR shifts (47 nm) with the alteration of the flow rates. Since the composition of the Cu_{2-x}S NCs obtained by the variation of the flow rates exhibited only two similar structures as covellite ($\text{Cu}_{1.1}\text{S}$) and spionkopite ($\text{Cu}_{1.39}\text{S}$), so that the shifting of the LSPR spectra might not be influenced by the compositions of the Cu_{2-x}S NCs. The relative small amount of LSPR shifting might be attributed to the effect of the size-dependent of Cu_{2-x}S NCs, as suggested by Luther et al. [2] and Saldanha et al. [83]. Besides, the shifting of the LSPR peaks was shown more obviously with a total of 529 nm (1115 nm-1644 nm), as the incline of the molar ratio between the copper to sulfur precursors. It is known that the positions of the LSPR spectra are closely associated with the stoichiometry level of the Cu_{2-x}S NCs, which is the x -value in the Cu_{2-x}S NCs. As the larger of the x -value of the Cu_{2-x}S NCs implies the higher copper-deficiency level, the higher density of the free holes could be found in the nanocrystals, resulting the blue-shift of the LSPR spectra. This alterable plasmonic property was also reported by Kriegel and Xie [3, 7], who have demonstrated the reversible tuning of the LSPR spectrum through the redox reaction on the Cu_{2-x}S NCs. On the other hand, it was found that the shifts of the LSPR spectrum were not significantly influenced by the shape or the size of the Cu_{2-x}S NCs. This might be

attributed to the relative small changes of aspect ratio (1.1 to 3.4) and diameter (6.4 nm to 12.6 nm) among the Cu_{2-x}S NCs batches. It is believed the varied morphologies among the Cu_{2-x}S NCs were not the main contributor in terms of the shift of LSPR. Another focus from LSPR finding is the relative broad full-width-half-maximum (FWHM) among the samples. It was generally believed that the uncommon wide FWHM was attributed to the poly-crystal structure of Cu_{2-x}S NCs. As suggested by Alivisatos's group [2], Burda's group [1] and Liu's group [6], this vast FWHM of LSPR was the product of the poly-crystal structure from the Cu_{2-x}S NCs. As mentioned in the previous section, the increased molar ratio between the precursors brought a series of $\text{Cu}_{1.1}\text{S}$ NCs, $\text{Cu}_{1.39}\text{S}$ NCs, $\text{Cu}_{1.75}\text{S}$ NCs and $\text{Cu}_{1.97}\text{S}$ NCs. Those compositions of nanocrystals could be understood and represented by a list of x -value as 0.9, 0.61, 0.25 and 0.03. As a result, the LSPR spectra among different molar ratios have exhibited a red-shift in the NIR region.

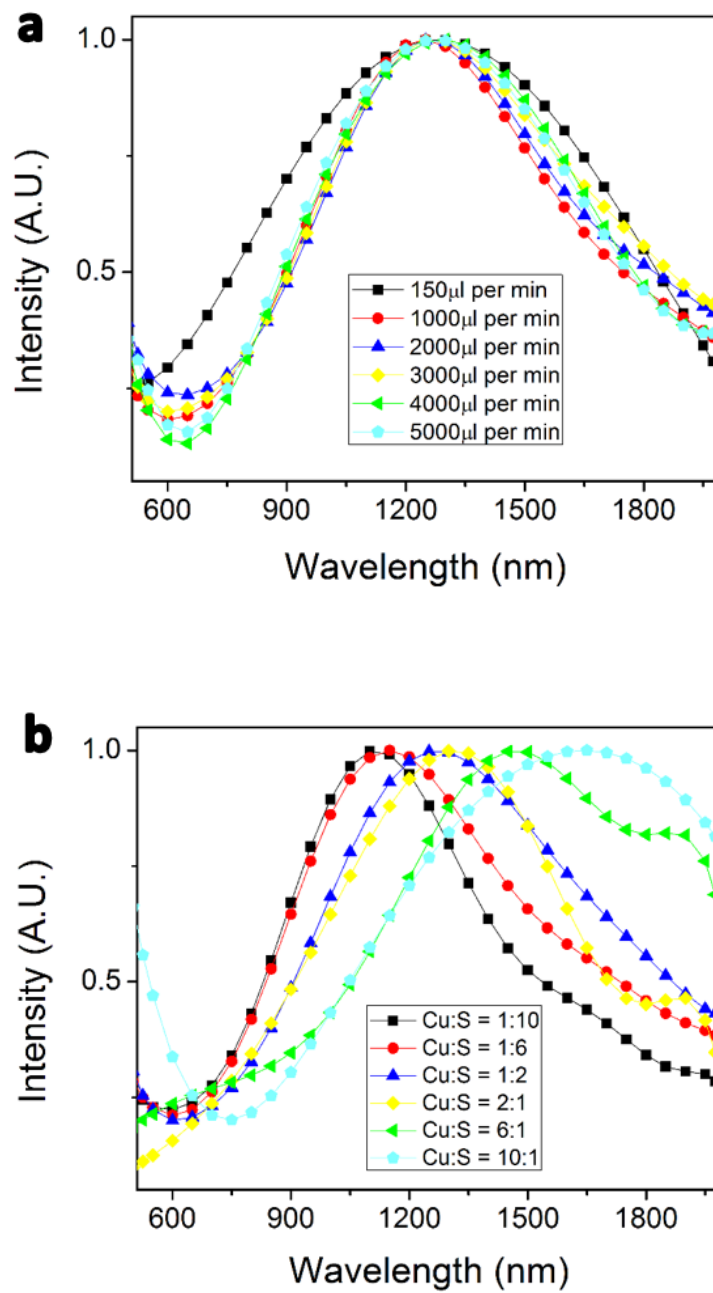


Figure 20 Absorption spectra of the Cu_{2-x}S NCs by varying a) different flow rates and b) precursors' concentration.

4.2 The Results of the Plasmonic Property in a variety of Morphologies and Compositions of Cu_{2-x}S NCs

4.2.1 Organic Environment

The result for different refractive index organic solvents to the shift of LSPR peaks for different compositions of Cu_{2-x}S NCs is shown as Figure 21. Four different compositions of Cu_{2-x}S NCs (i.e. $\text{Cu}_{1.1}\text{S}$, $\text{Cu}_{1.39}\text{S}$, $\text{Cu}_{1.75}\text{S}$ and $\text{Cu}_{1.97}\text{S}$) exhibited different signal response ratios in the LSPR peaks shift due to their different levels of copper-deficiency. This result revealed that different compositions of Cu_{2-x}S NCs provided different level of responses to the external change of the refractive index medium. However, since it was difficult to provide a gradient change of the refractive index medium in organic solvents, the calibration curves among different morphologies and compositions of Cu_{2-x}S NCs were obtained in the aqueous environment study.

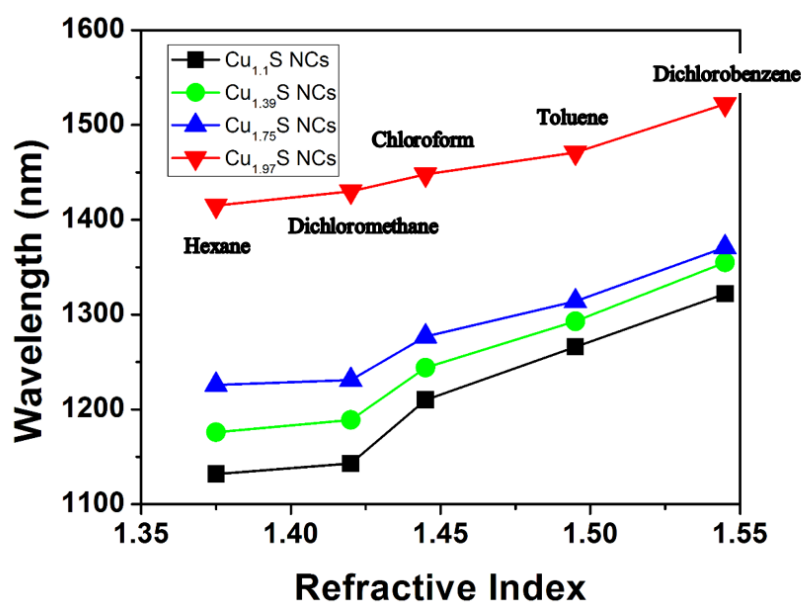


Figure 21 Responses of the LSPR peaks Cu_{2-x}S NCs upon different organic solvents with a ranged of refractive index.

4.2.2 Aqueous Environment

Different sizes, aspect ratios and compositions of Cu_{2-x}S NCs are shown in Figure 22. Figure 22a shows that all the spherical $\text{Cu}_{1.39}\text{S}$ NCs with size 3.6 nm, 6.4 nm and 12.6 nm exhibited different signal response change of LSPR peaks shifting depended on different glycerin-water ratios. In Table 3, the LSPR peaks shifted are listed per each percentage of glycerin-water ratio and the refractive index unit (RIU). 3.6 nm, 6.4 nm and 12.6 nm sized spherical $\text{Cu}_{1.39}\text{S}$ NCs showed 1.18, 1.00 and 0.80 nm shifted per each percentage of glycerin-water ratio, and 850, 714 and 573 nm shifted per RIU respectively. For different aspect ratios of the rod-shaped $\text{Cu}_{1.1}\text{S}$ NCs, aspect ratio of 1.1, 2.3 and 3.4 nanocrystals resulted in 1.00, 1.18 and 1.38 nm shift per each percentage of glycerin-water ratio, and 714, 842 and 985 nm shifted per RIU respectively. Finally, for the four different compositions of the 8.8 nm spherical Cu_{2-x}S NCs, $\text{Cu}_{1.1}\text{S}$, $\text{Cu}_{1.39}\text{S}$, $\text{Cu}_{1.75}\text{S}$ and $\text{Cu}_{1.97}\text{S}$ NCs showed 1.00, 0.88, 0.65 and 0.54 nm shift per each percentage of glycerin-water ratio, and 714, 629, 464 and 386 nm shift per RIU respectively. These results have revealed that the rod-shaped $\text{Cu}_{1.1}\text{S}$ NCs with the largest aspect ratio of 3.4 has the highest sensitivity. This might be attributed to the largest copper-deficiency of covellite structure Cu_{2-x}S NCs, which consisted of the highest carrier density and number of free holes. In addition, since the largest aspect ratio of the nanocrystals have a better sharpness on the edges, where more plasmonics might be confined, and thereby exhibited a higher sensitivity [84, 85].

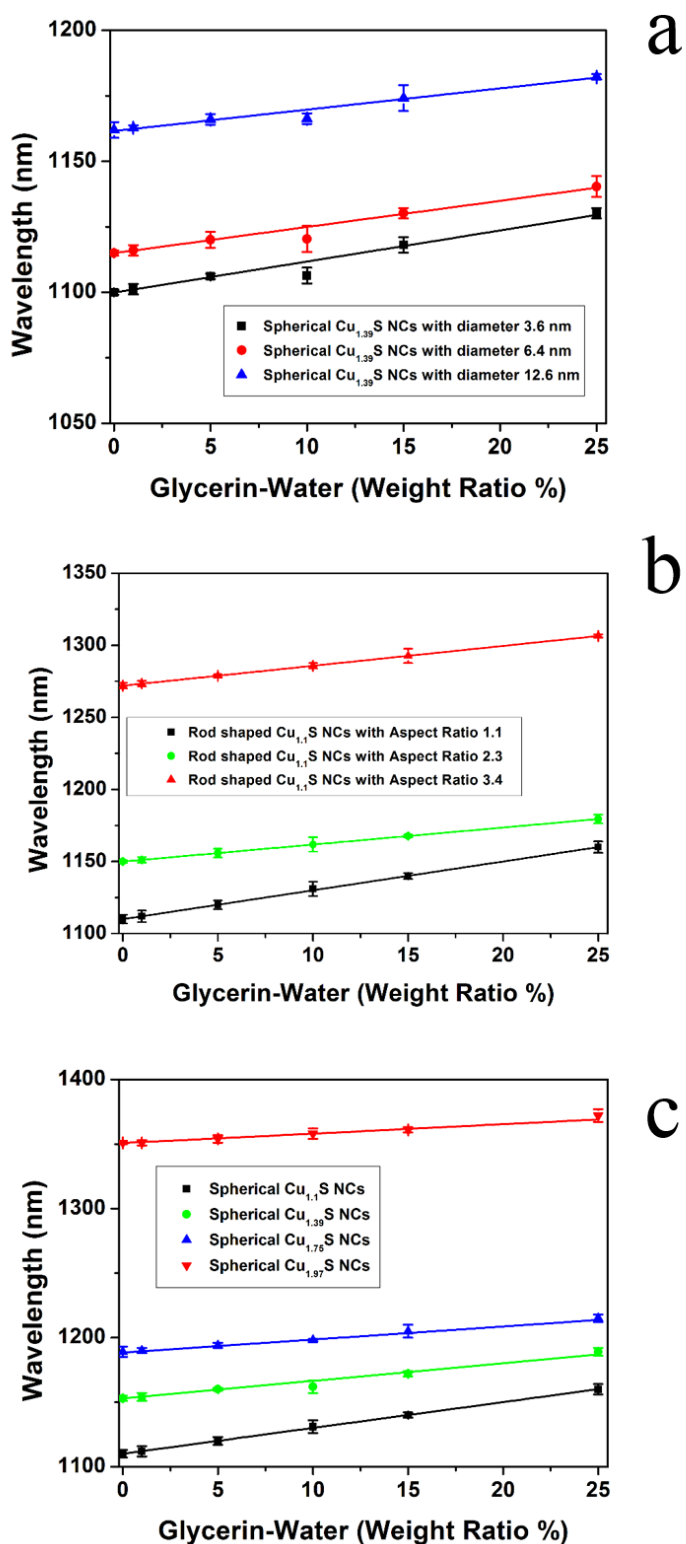


Figure 22 The effect of a variety of glycerin-water ratios to the LSPR peaks by different a) sizes b) aspect ratios and c) compositions of Cu_{2-x}S NCs.

Table 3 The LSPR peaks shifted per each percentage of glycerin-water ratio and the refractive index unit (RIU) of different a) size b) aspect ratios and c) compositions of Cu_{2-x}S NCs by a variety of glycerin-water ratios.

$\text{Cu}_{1.39}\text{S}$ NCs with diameter 3.6 nm		$\text{Cu}_{1.39}\text{S}$ NCs with diameter 6.4 nm		$\text{Cu}_{1.39}\text{S}$ NCs with diameter 12.6 nm	
1.18 nm / % Glycerin 850 nm / RIU		1.00 nm / % Glycerin 714 nm / RIU		0.80 nm / % Glycerin 573 nm / RIU	
Rod-shaped $\text{Cu}_{1.1}\text{S}$ Aspect Ratio 1.1		Rod-shaped $\text{Cu}_{1.1}\text{S}$ Aspect Ratio 2.3		Rod-shaped $\text{Cu}_{1.1}\text{S}$ Aspect Ratio 3.4	
1.00 nm / % Glycerin 714 nm / RIU		1.18 nm / % Glycerin 842 nm / RIU		1.38 nm / % Glycerin 985 nm / RIU	
Spherical $\text{Cu}_{1.1}\text{S}$ NCs with diameter 8 nm	Spherical $\text{Cu}_{1.39}\text{S}$ NCs with diameter 8.8 nm	Spherical $\text{Cu}_{1.75}\text{S}$ NCs with diameter 8.8 nm	Spherical $\text{Cu}_{1.97}\text{S}$ NCs with diameter 12.0 nm		
1.00 nm / % Glycerin 714 nm / RIU	0.88 nm / % Glycerin 629 nm / RIU	0.65 nm / % Glycerin 464 nm / RIU	0.54 nm / % Glycerin 386 nm / RIU		

4.3 Plasmonic Quenching Effect and the Fluorescence Enhancement by Different Ratios between Cu_{2-x}S NCs and OPD in a Variety of Morphologies and Compositions of the Cu_{2-x}S NCs

Since the plasmonic property of the heavily-doped semiconductor Cu_{2-x}S NCs could be altered by the number of free holes, when it reacted with the OPD compound, the electrons trapped the holes of Cu_{2-x}S NCs, thus resulting in the plasmonic quenching. As mentioned in the previous section, different sizes, aspect ratios and compositions of Cu_{2-x}S NCs exhibited different level of sensitivity due to their distinct number of holes. Similarly, the distinct number of holes in Cu_{2-x}S NCs could lead in different plasmonic quenching effect. On the other hand, as the oxidized OPD could emit fluorescence, the fluorescence could be enhanced individually by disparate sizes, aspect ratios and compositions of Cu_{2-x}S NCs. This section will discuss on the plasmonic quenching and then the fluorescence enhancement. Figure 23 has shown the color change of different ratios between Cu_{2-x}S NCs (ppm) and the OPD (ppm) ranging from (0 : 21600), (650 : 21600), (650 : 10800), (650 : 216) and (650 : 0).

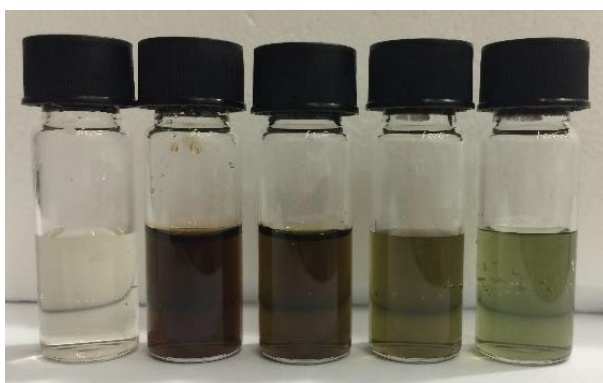


Figure 23 Digital photos on different ratios between Cu_{2-x}S NCs (ppm) and the OPD (ppm) started from the leftmost (0 : 21600), (650 : 21600), (650 : 10800), (650 : 216) and (650 : 0).

4.3.1 Plasmonic Quenching Effect

The study on the plasmonic quenching effect has been divided into three different parts by the disparate sizes, aspect ratios and compositions of Cu_{2-x}S NCs as shown in Figure 24, Figure 25 and Figure 26 respectively. Table 4 has listed out the quenching effect for disparate sizes of spherical $\text{Cu}_{1.39}\text{S}$ NCs by measuring the intensity of the LSPR peaks under a variety of OPD amount. It has revealed that the smallest sized nanoparticles exhibited the largest quenching amplitude of 94 % when 21600 ppm of OPD adding into the Cu_{2-x}S NCs. This might be attributed to the higher sensitive of the small size nanoparticles, which was similar to the case of the gold nanoparticles [86]. Table 5 shows the quenching effect on different aspect ratio of the rod-shaped $\text{Cu}_{1.1}\text{S}$ NCs by similar measurement. It has showed that the largest aspect ratio (i.e. 3.4) exhibited the largest quenching amplitude of 89 % as 21600 ppm of OPD adding into the Cu_{2-x}S NCs. Similar finding also suggested by the different rod-shaped gold nanoparticles. This indicated that the largest aspect ratio exhibited the highest sensitivity [71]. Table 6 lists out quenching effect on different compositions of the 8.8 nm spherical Cu_{2-x}S NCs obtained by conducting the LSPR peaks measurement. Similarly, it has showed that the 8.8 nm spherical $\text{Cu}_{1.1}\text{S}$ NCs exhibited the largest quenching amplitude of 74 % when it reacted with 21600 ppm of OPD. This might be attributed to the stronger absorption intensity by $\text{Cu}_{1.1}\text{S}$ NCs comparing to the lower copper-deficiency nanocrystals which were $\text{Cu}_{1.39}\text{S}$ NCs, $\text{Cu}_{1.75}\text{S}$ NCs and $\text{Cu}_{1.97}\text{S}$ NCs, as reported by Alivisatos's group previously [2].

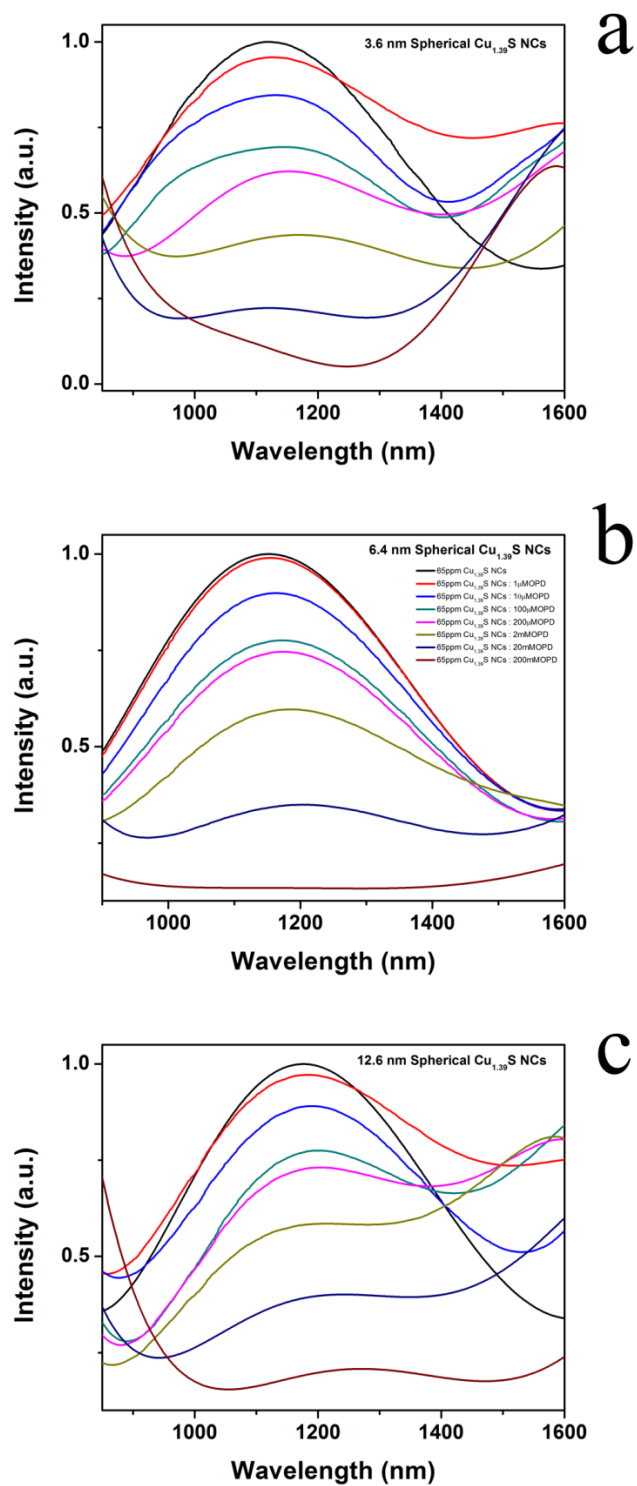


Figure 24 Plasmonic quenching of different sized spherical $\text{Cu}_{1.39}\text{S}$ NCs for a) 3.6 nm b) 6.4 nm and c) 12.6 nm. The black line indicates the 65 ppm spherical $\text{Cu}_{1.39}\text{S}$ NCs. The following red, light blue, green, purple, light brown, navy blue and dark brown lines indicates different OPD (ppm) amount from 0.108, 1.08, 10.8, 21.6, 216, 2160 and 21600 respectively.

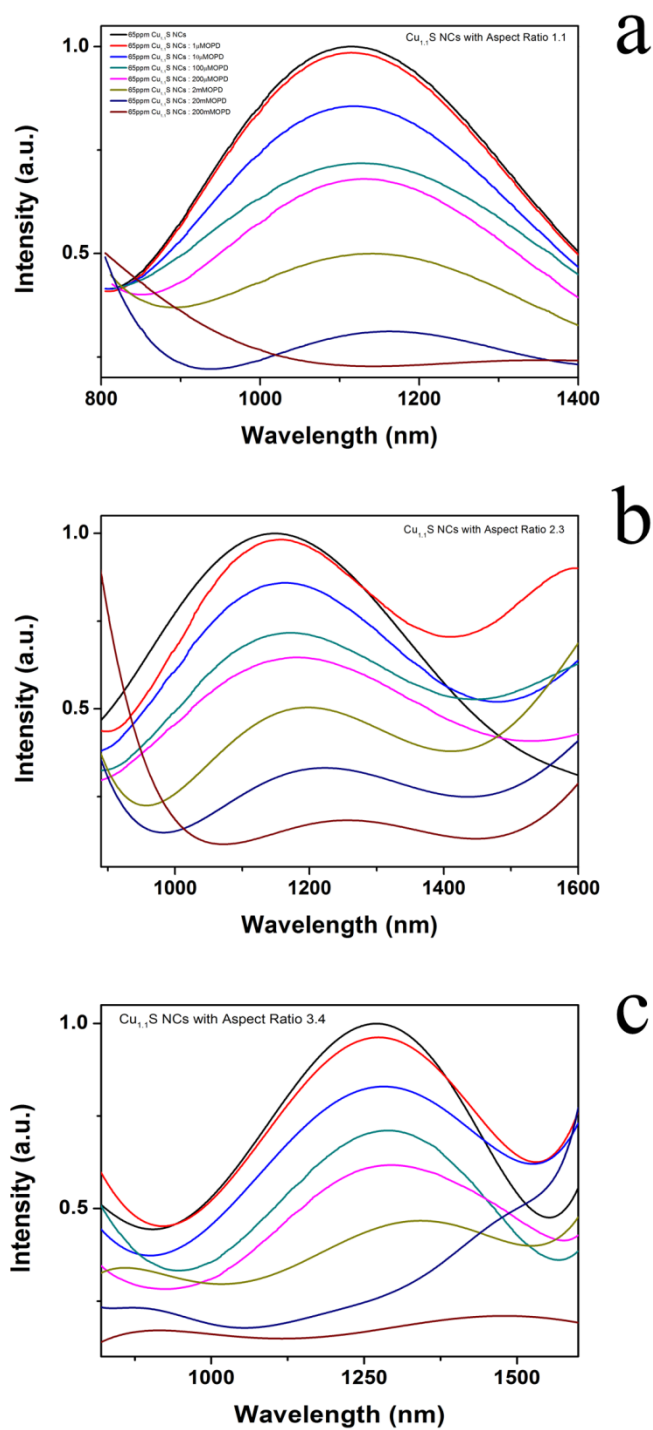
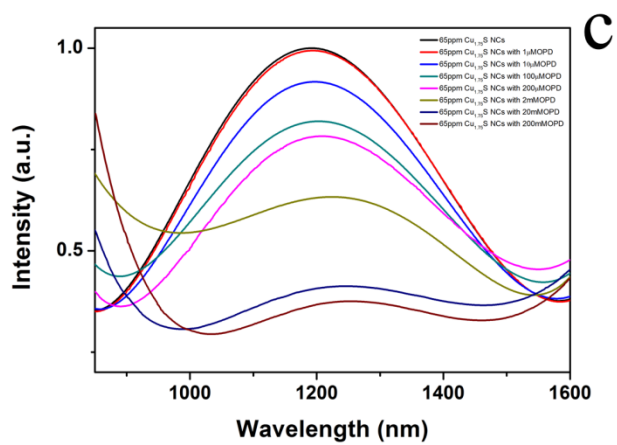
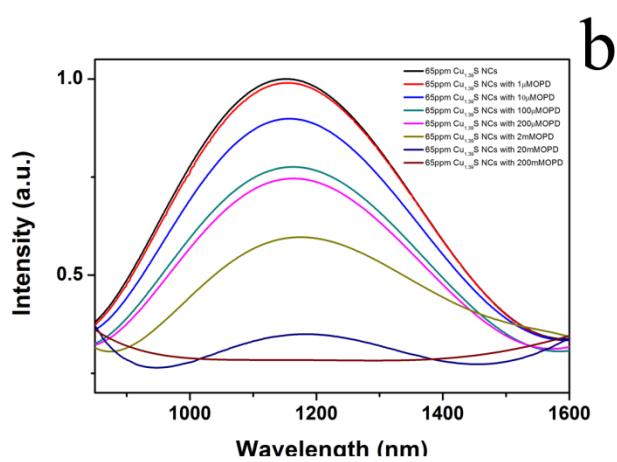
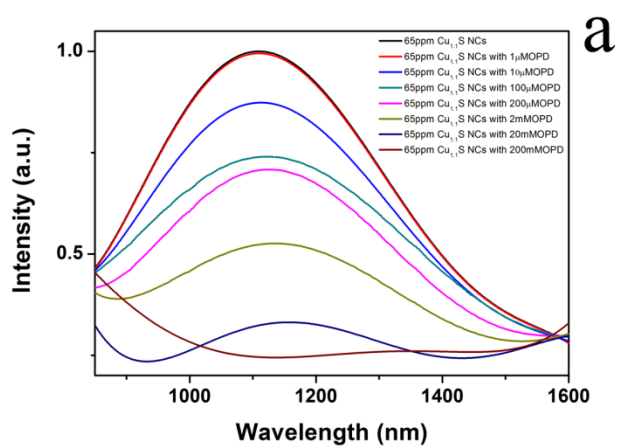


Figure 25 Plasmonic quenching of different aspect ratios of the rod-shaped $\text{Cu}_{1.1}\text{S}$ NCs for a) 1.1 b) 2.3 and c) 3.4. The black line indicates the 65 ppm rod-shaped $\text{Cu}_{1.1}\text{S}$ NCs. The following red, light blue, green, purple, light brown, navy blue and dark brown lines indicates different OPD (ppm) amount from 0.108, 1.08, 10.8, 21.6, 216, 2160 and 21600 respectively.



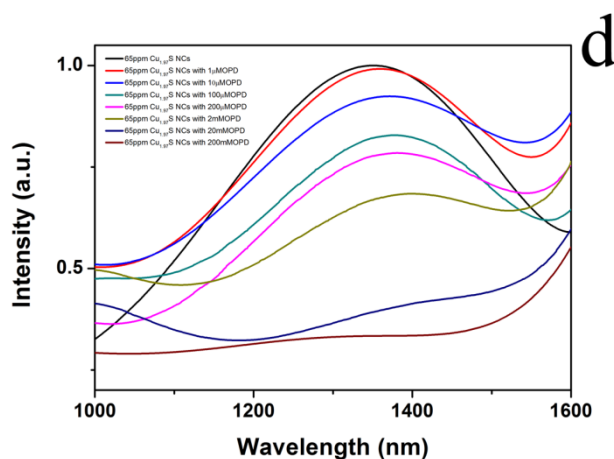


Figure 26 Plasmonic quenching of different compositions of the 8.8 nm spherical Cu_{2-x}S NCs for a) $\text{Cu}_{1.1}\text{S}$ b) $\text{Cu}_{1.39}\text{S}$ c) $\text{Cu}_{1.75}\text{S}$ and d) $\text{Cu}_{1.97}\text{S}$. The black line indicates the 65 ppm rod-shaped Cu_{2-x}S NCs. The following red, light blue, green, purple, light brown, navy blue and dark brown lines indicates different OPD (ppm) amount from 0.108, 1.08, 10.8, 21.6, 216, 2160 and 21600 respectively.

Table 4 Plasmonic quenching effect on different sized spherical $\text{Cu}_{1.39}\text{S}$ NCs by measuring the intensity of the LSPR peaks under a variety of OPD amount.

OPD (ppm)	Quenching effect on 3.6 nm spherical $\text{Cu}_{1.39}\text{S}$ NCs	Quenching effect on 6.4 nm spherical $\text{Cu}_{1.39}\text{S}$ NCs	Quenching effect on 12.6 nm spherical $\text{Cu}_{1.39}\text{S}$ NCs
0.108	0.05	0.01	0.03
1.08	0.16	0.10	0.11
10.8	0.31	0.22	0.22
21.6	0.38	0.27	0.27
216	0.56	0.41	0.41
2160	0.78	0.60	0.60
21600	0.94	0.79	0.79

Table 5 Plasmonic quenching effect on different aspect ratios of the rod-shaped $\text{Cu}_{1.1}\text{S}$ NCs by measuring the intensity of the LSPR peaks under a variety of OPD amount.

OPD (ppm)	Quenching effect of the rod-shaped $\text{Cu}_{1.1}\text{S}$ NCs with aspect Ratio 1.1	Quenching effect of the rod-shaped $\text{Cu}_{1.1}\text{S}$ NCs with aspect Ratio 2.3	Quenching effect of the rod-shaped $\text{Cu}_{1.1}\text{S}$ NCs with aspect Ratio 3.4
0.108	0.02	0.02	0.04
1.08	0.14	0.14	0.17
10.8	0.28	0.28	0.29
21.6	0.32	0.35	0.38
216	0.5	0.5	0.53
2160	0.67	0.67	0.79
21600	0.74	0.82	0.89

Table 6 Plasmonic quenching effect on different compositions of the 8.8 nm spherical Cu_{2-x}S NCs by measuring the intensity of the LSPR peaks under a variety of OPD amount.

OPD (ppm)	Quenching effect on the 8.8 nm spherical $\text{Cu}_{1.1}\text{S}$ NCs	Quenching effect on the 8.8 nm spherical $\text{Cu}_{1.39}\text{S}$ NCs	Quenching effect on the 8.8 nm spherical $\text{Cu}_{1.75}\text{S}$ NCs	Quenching effect on the 8.8 nm spherical $\text{Cu}_{1.97}\text{S}$ NCs
0.108	0.01	0.01	0.01	0.01
1.08	0.13	0.10	0.08	0.08
10.8	0.26	0.22	0.18	0.17
21.6	0.29	0.25	0.22	0.22
216	0.47	0.40	0.37	0.32
2160	0.67	0.65	0.59	0.65
21600	0.74	0.72	0.62	0.67

4.3.2 Fluorescence Enhancement

The study of fluorescence enhancement is divided into three different parts by the disparate sizes, aspect ratios and compositions of Cu_{2-x}S NCs as shown in Figure 27, Figure 28 and Figure 29 respectively. Table 7 shows the fluorescence enhancement for different sizes of spherical $\text{Cu}_{1.39}\text{S}$ NCs by measuring and comparing the intensity of the fluorescence peaks at 568 nm under a variety of OPD amount. It has revealed that the smallest sized nanoparticles exhibited the largest enhancement of 983×10^3 when 216 ppm of OPD adding into the 65 ppm $\text{Cu}_{1.39}\text{S}$ NCs. This demonstrated that when the ratio between Cu_{2-x}S NCs and the OPD reached around 0.3, the fluorescence enhancement is optimized. The lowest enhancement amplitude is 4.5×10^3 , which was contributed to the ratio of 65 ppm of $\text{Cu}_{1.39}\text{S}$ NCs to 0.108 ppm OPD. Since the lowest fluorescence enhancement achieved 4.5×10^3 and the fluorescence intensity of the 0.108 ppm OPD was only 0.02×10^3 , therefore the minimum signal-to-noise ratio was around 225 times which has satisfied a typical signal-to-noise requirement of a sensor [27, 29]. Table 8 reports the fluorescence enhancement for different aspect ratio of the rod-shaped $\text{Cu}_{1.1}\text{S}$ NCs by similar measurement on the intensity of the fluorescence peaks at 568 nm under a variety of OPD amount. This result reveals that the largest aspect ratio (i.e. 3.4) of rod-shaped $\text{Cu}_{1.1}\text{S}$ NCs exhibited the largest enhancement of 1100×10^3 when 216 ppm of OPD was added into the 65 ppm rod-shaped $\text{Cu}_{1.1}\text{S}$ NCs, on the other word, when the ratio between the Cu_{2-x}S NCs and the OPD molecule reached around 0.3, the fluorescence was enhanced to the largest signal-to-noise ratio. The lowest enhancement amplitude is 1.3×10^3 , which was contributed to the ratio of 65 ppm of $\text{Cu}_{1.39}\text{S}$ NCs to 0.108 ppm OPD. Since the fluorescence intensity of the 0.108 ppm OPD was around 0.02×10^3 , this lowest enhancement satisfied previous by discussed signal-to-noise of the

typical sensors. Finally, Table 9 shows the fluorescence enhancement for different compositions of the 8.8 nm spherical Cu_{2-x}S NCs obtained by same fluorescence measurement. This result reveals that the $\text{Cu}_{1.1}\text{S}$ NCs exhibits the largest enhancement of 910×10^3 among the other lower copper-deficiency Cu_{2-x}S NCs when the ratio between $\text{Cu}_{1.1}\text{S}$ NCs and the OPD reached around 0.3. For the sample of 0.108 ppm OPD with Cu_{2-x}S NCs, it reveals the lowest enhancement amplitude of 0.2×10^3 .

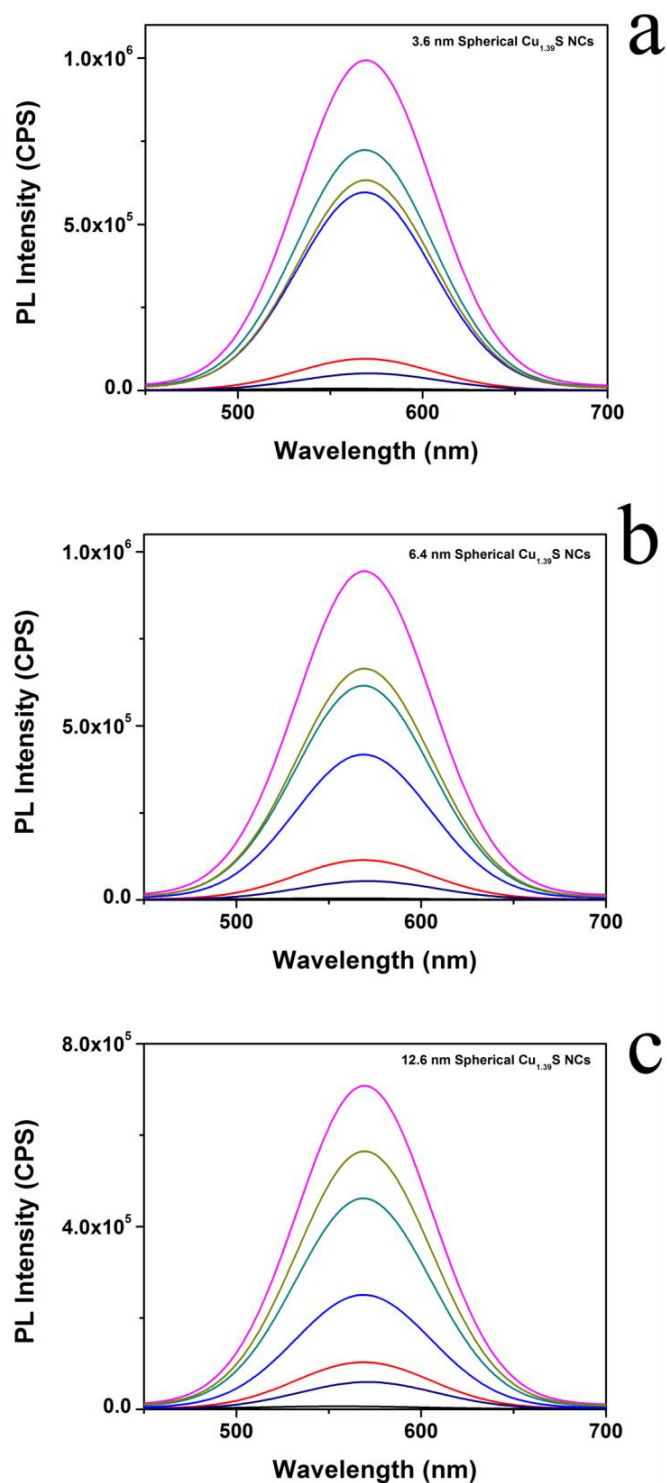


Figure 27 Enhanced fluorescence intensity under different size spherical $\text{Cu}_{1.39}\text{S}$ NCs for a) 3.6 nm b) 6.4 nm and c) 12.6 nm. The black, red, blue, green, purple, light brown and the navy blue lines indicate different ratios of $\text{Cu}_{1.39}\text{S}$ NCs to OPD ranging from 600, 60, 6, 3, 0.3, 0.03 and 0.003, respectively.

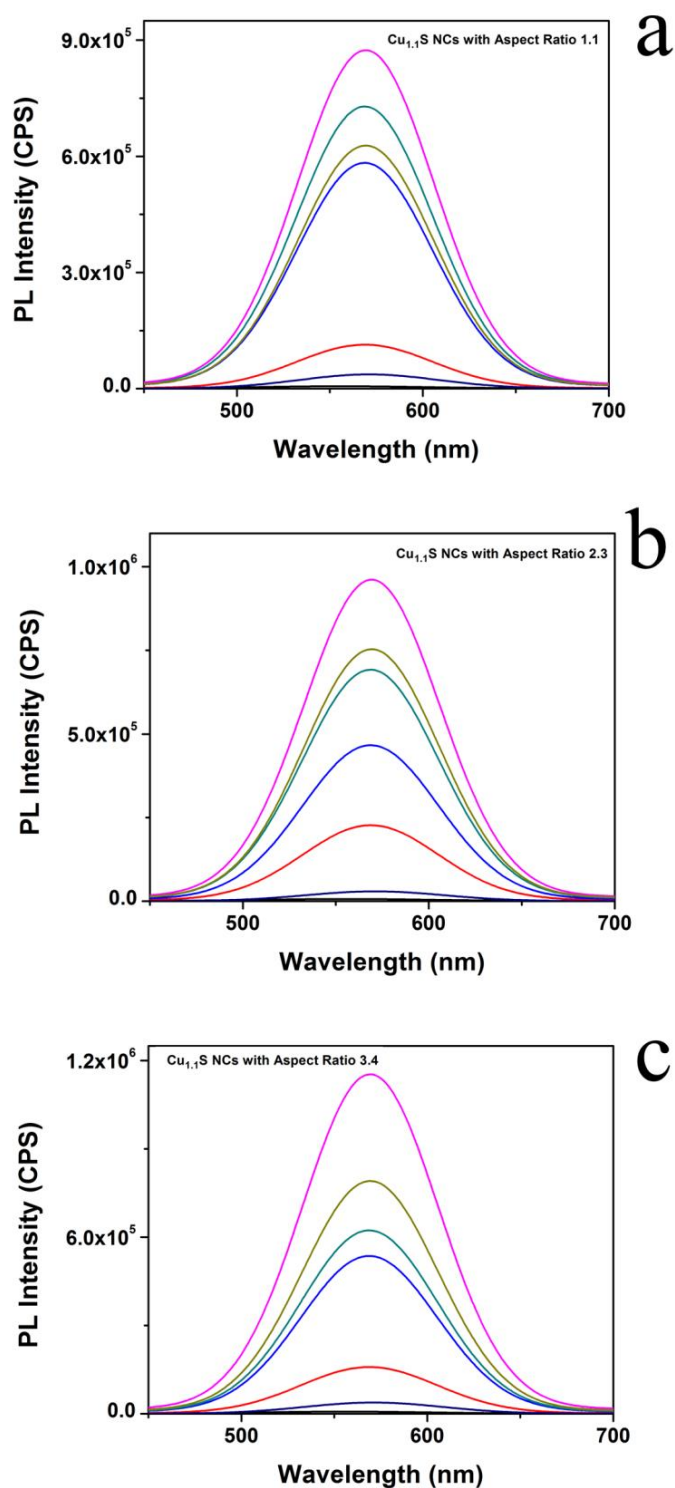
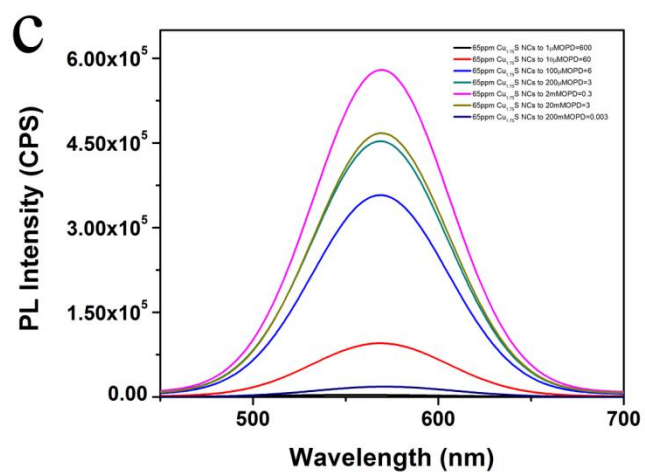
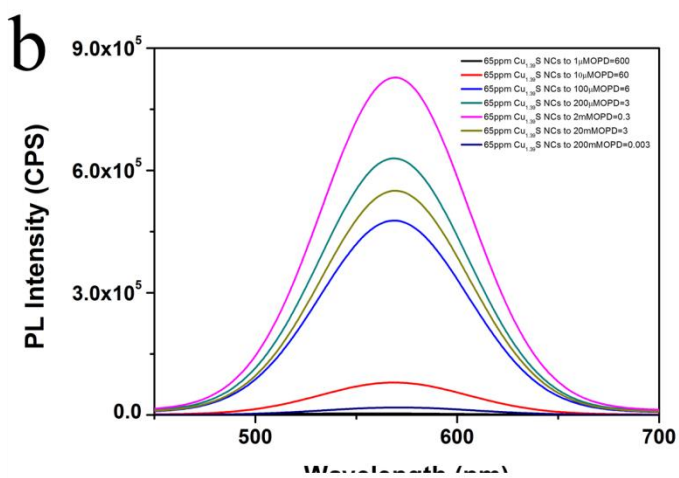
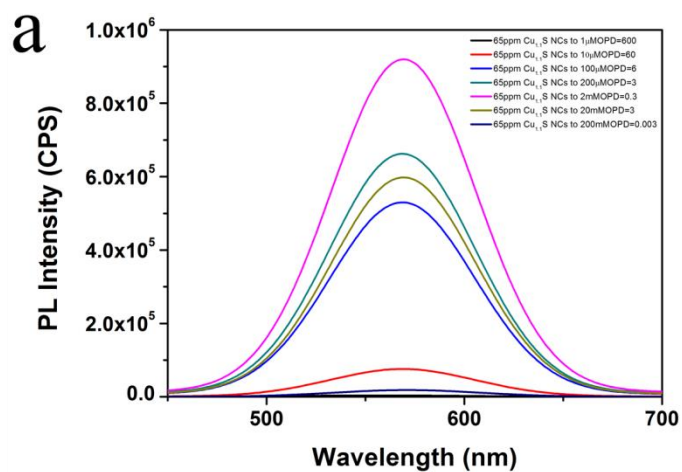


Figure 28 Enhanced fluorescence intensity under different aspect ratios of the rod-shaped $\text{Cu}_{1.1}\text{S}$ NCs for a) 1.1 b) 2.3 and c) 3.4. The black, red, blue, green, purple, light brown and the navy blue lines indicate different ratios of $\text{Cu}_{1.39}\text{S}$ NCs to OPD ranging from 600, 60, 6, 3, 0.3, 0.03 and 0.003, respectively.



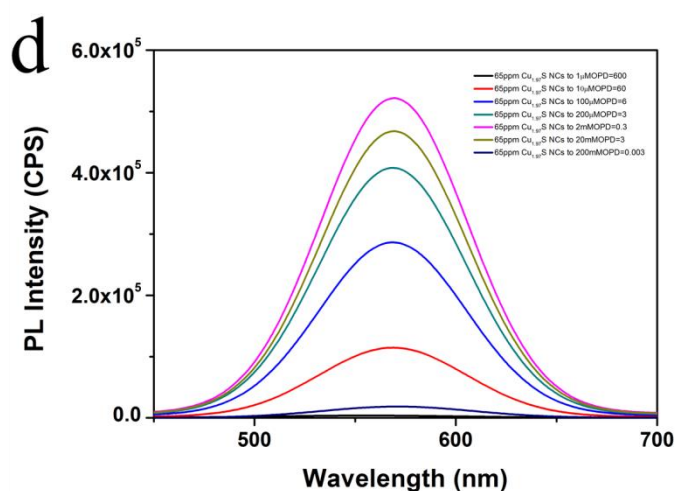


Figure 29 Enhanced fluorescence intensity of different compositions of the 8.8 nm spherical Cu_{2-x}S NCs for a) $\text{Cu}_{1.1}\text{S}$ b) $\text{Cu}_{1.39}\text{S}$ c) $\text{Cu}_{1.75}\text{S}$ and d) $\text{Cu}_{1.97}\text{S}$. The black, red, blue, green, purple, light brown and the navy blue lines indicate different ratios of $\text{Cu}_{1.39}\text{S}$ NCs to OPD ranging from 600, 60, 6, 3, 0.3, 0.03 and 0.003, respectively.

Table 7 Enhanced fluorescence intensity on different sized spherical $\text{Cu}_{1.39}\text{S}$ NCs by measuring the intensity of the fluorescence peaks at 568 nm under a variety of OPD amount.

OPD (ppm)	Fluorescence enhancement on 3.6 nm spherical $\text{Cu}_{1.39}\text{S}$ NCs ($\times 10^3$)	Fluorescence enhancement on 6.4 nm spherical $\text{Cu}_{1.39}\text{S}$ NCs ($\times 10^3$)	Fluorescence enhancement on 12.6 nm spherical $\text{Cu}_{1.39}\text{S}$ NCs ($\times 10^3$)
0.108	5.60	4.50	6.30
1.08	95.2	114	103
10.8	594	415	248
21.6	719	611	456
216	983	934	698
2160	618	650	550
21600	33.5	36.0	41.0

Table 8 Enhanced fluorescence intensity on different aspect ratios of the rod-shaped $\text{Cu}_{1.1}\text{S}$ NCs by measuring the intensity of the fluorescence peaks at 568 nm under a variety of OPD amount.

OPD (ppm)	Fluorescence enhancement of the rod-shaped $\text{Cu}_{1.1}\text{S}$ NCs with aspect Ratio 1.1 ($\times 10^3$)	Fluorescence enhancement of the rod-shaped $\text{Cu}_{1.1}\text{S}$ NCs with aspect Ratio 2.3 ($\times 10^3$)	Fluorescence enhancement of the rod-shaped $\text{Cu}_{1.1}\text{S}$ NCs with aspect Ratio 3.4 ($\times 10^3$)
0.108	6.00	6.60	1.30
1.08	113	227	159
10.8	581	464	534
21.6	724	687	618
216	864	951	1100
2160	613	739	776
21600	18.7	11.3	20.2

Table 9 Enhanced fluorescence intensity on different compositions of the 8.8 nm spherical Cu_{2-x}S NCs by measuring the intensity of the fluorescence peaks at 568 nm under a variety of OPD amount.

OPD (ppm)	Fluorescence enhancement on the 8.8 nm spherical $\text{Cu}_{1.1}\text{S}$ NCs ($\times 10^3$)	Fluorescence enhancement on the 8.8 nm spherical $\text{Cu}_{1.39}\text{S}$ NCs ($\times 10^3$)	Fluorescence enhancement on the 8.8 nm spherical $\text{Cu}_{1.75}\text{S}$ NCs ($\times 10^3$)	Fluorescence enhancement on the 8.8 nm spherical $\text{Cu}_{1.97}\text{S}$ NCs ($\times 10^3$)
0.108	3.70	3.70	3.70	3.00
1.08	75.5	79.3	95.2	114
10.8	528	475	356	284
21.6	657	624	448	403
216	910	818	569	512
2160	583	535	453	453
21600	0.20	0.20	0.20	0.20

Chapter 5 Conclusions and Future Work

This dissertation has studied the nanomanufacturing of plasmonic material, which was the copper-based semiconductor nanocrystal (Cu_{2-x}S NCs). This plasmonic material is getting attention since its plasmonic property is originated from its abundant number of free holes. Due to its unique feature, Cu_{2-x}S NCs are capable to extend the plasmonic sensitivity from the surrounding environment as compared to the metallic nanoparticles. Typically, the sensitivity of the plasmonic material not only depends on the type of material, but also on the morphology and nonstoichiometric composition of the nanoparticles. However, there is little empirical research work found in the semiconductor Cu_{2-x}S NCs as there is only a limited number of studies demonstrating the control of the size, shape and composition of Cu_{2-x}S NCs, though some results were achieved with the assist of a highly toxic surfactant. Our study was attempted to satisfy these research needs and study this unique plasmonic properties.

In order to control the size, shape and composition of Cu_{2-x}S NCs, this study exploited a continuous-flow millifluidic device as a nanomanufacturing tool for Cu_{2-x}S NCs fabrication. This millifluidic on-chip fabrication offered an ideal incubation platform for the growth of nanoparticles. For instance, the large surface area to volume ratio of the chip allowed heat to be distributed uniformly during the synthesis. In addition, the relative large channel sizes could enhance the production rate and enabled the potential scaled-up production. Furthermore, nanoparticles synthesized in laminar flow were highly consistent since the continuous-flow fluidic could ensure the stoichiometry ratio between precursors and allowed a precise control of reaction time. This nanomanufacturing platform enabled the fine-tuning of

nanoparticles for specific needs in sensing. Therefore, it is a valuable option to use the millifluidic on-chip fabrication to synthesize the Cu_{2-x}S NCs.

The as-synthesized Cu_{2-x}S NCs were characterized by the scanning transmission electron microscope (STEM), powder X-ray diffraction (XRD), Energy-dispersive X-ray spectroscopy (EDX), inductively coupled plasma - optical emission spectrometry (ICP-OES) and the UV-Vis-NIR spectroscopy. It has been revealed that through the control of the input flow rates. It is manageable to fabricate spherical Cu_{2-x}S NCs with 3.6 – 12.6 nm and rod-shaped Cu_{2-x}S NCs with aspect ratio 2.3 – 3.4. Moreover, by altering the molar ratios between precursors, it was possible to fabricate four different compositions of Cu_{2-x}S NCs including $\text{Cu}_{1.1}\text{S}$, $\text{Cu}_{1.39}\text{S}$, $\text{Cu}_{1.75}\text{S}$ and $\text{Cu}_{1.97}\text{S}$.

The study included the investigation of the plasmonic properties of a various morphologies and compositions of Cu_{2-x}S NCs. Firstly, the study was focused on the localized surface plasmonic resonance (LSPR) property of the Cu_{2-x}S NCs exposed under different refractive index media by dispersing the Cu_{2-x}S NCs into a variety of glycerin-water weight ratios. It has shown that those four different compositions of Cu_{2-x}S NCs gave a range of responses of 386 nm / RIU to 714 nm / RIU, while different aspect ratios (1.1 to 3.4) of the rod-shaped Cu_{2-x}S NCs exhibited 714 nm / RIU to 985 nm / RIU and different sizes (3.6 nm to 12.6 nm) of Cu_{2-x}S NCs give 573 nm / RIU to 850 nm / RIU. Furthermore, we have investigated the plasmonic quenching effect through the redox reaction between the oxidation o-phenyldiamine (OPD) and the reduction / holes trapping of Cu_{2-x}S NCs. As the oxidized OPD compound was able to emit the yellow fluorescence at around 568 nm, the studied has also discussed on the effect of the fluorescence enhancement under

different molar ratio between Cu_{2-x}S NCs to OPD. The results showed that the LSPR absorption was quenched as the molar ratio between the Cu_{2-x}S NCs to OPD decreased from 600 (excessive Cu_{2-x}S NCs) to 0.003 (excessive OPD). On the other hand, the fluorescence was enhanced ranging from 0.2×10^3 to 1.1×10^6 , depending on different morphologies, compositions and the precursor's concentration between Cu_{2-x}S NCs to OPD. It was found that the rod-shaped Cu_{2-x}S NCs with aspect ratio 3.4 exhibited the largest fluorescence enhancement at 1.1×10^6 . All the Cu_{2-x}S NCs / OPD samples revealed that the fluorescence enhancement was optimized when their molar ratios reached around at 0.3 (Cu_{2-x}S NCs to OPD), which excessive Cu_{2-x}S NCs or OPD resulted on a weaker fluorescence emission. This result suggests a satisfying signal-to-noise value for the Cu_{2-x}S NCs based nanosensor.

The future work can be divided into two parts. (i) the development and application of the nanomanufacturing platform, and (ii) the study on the Raman resonance for a variety of morphologies and compositions of Cu_{2-x}S NCs. This dissertation has demonstrated the potential ability of the modification on the morphologies and compositions for nanoparticles, without the use of other toxic surfactants. This platform can be further explored on the other nanoparticles fabrication such as quantum dots and the metallic nanoparticles. Moreover, the nanomanufacturing platform can be manageable on the complex nanoparticles fabrication such as the core-shell nanoparticles, while keeping a high quality of the nanoparticles and fine-tuning ability. Nanomanufacturing platform can satisfy the scale-up production of the nanoparticles and meet the increasing demand on the nanoparticles in industries.

The second part of the future work purposed is to conduct the study on the surface-enhanced Raman scattering (SERS) for a variety of morphologies and compositions

of Cu_{2-x}S NCs. Li et al. have demonstrated that the surface-enhanced Raman scattering on different shaped CuTe nanocrystals. It has revealed that the cubic-shaped CuTe nanocrystals have a better resonance than other shaped nanocrystals such as the nanoplates and the nanorods, since they have better sharpness on the edges of the nanocrystals [81]. This result can be a good reference for the study of the surface-enhanced Raman scattering for the variety of morphologies and compositions of Cu_{2-x}S NCs.

References

1. Zhao, Y., H. Pan, Y. Lou, X. Qiu, J. Zhu, and C. Burda, *Plasmonic Cu_{2-x}S nanocrystals: optical and structural properties of copper-deficient copper (I) sulfides*. Journal of the American Chemical Society, 2009. **131**(12): p. 4253-4261.
2. Luther, J.M., P.K. Jain, T. Ewers, and A.P. Alivisatos, *Localized surface plasmon resonances arising from free carriers in doped quantum dots*. Nature materials, 2011. **10**(5): p. 361-366.
3. Kriegel, I., C. Jiang, J. Rodríguez-Fernández, R.D. Schaller, D.V. Talapin, E. Da Como, and J. Feldmann, *Tuning the excitonic and plasmonic properties of copper chalcogenide nanocrystals*. Journal of the American Chemical Society, 2012. **134**(3): p. 1583-1590.
4. Hsu, S.-W., W. Bryks, and A.R. Tao, *Effects of Carrier Density and Shape on the Localized Surface Plasmon Resonances of Cu_{2-x}S Nanodisks*. Chemistry of Materials, 2012. **24**(19): p. 3765-3771.
5. Wei, T., Y. Liu, W. Dong, Y. Zhang, C. Huang, Y. Sun, X. Chen, and N. Dai, *Surface-dependent localized surface plasmon resonances in CuS nanodisks*. ACS applied materials & interfaces, 2013. **5**(21): p. 10473-10477.
6. Liu, X., X. Wang, B. Zhou, W.C. Law, A.N. Cartwright, and M.T. Swihart, *Size - Controlled Synthesis of Cu_{2-x}E (E= S, Se) Nanocrystals with Strong Tunable Near - Infrared Localized Surface Plasmon Resonance and High Conductivity in Thin Films*. Advanced Functional Materials, 2013. **23**(10): p. 1256-1264.

7. Xie, Y., A. Riedinger, M. Prato, A. Casu, A. Genovese, P. Guardia, S. Sottini, C. Sangregorio, K. Miszta, and S. Ghosh, *Copper sulfide nanocrystals with tunable composition by reduction of covellite nanocrystals with Cu⁺ ions*. Journal of the American Chemical Society, 2013. **135**(46): p. 17630-17637.
8. Alam, R., M. Labine, C.J. Karwacki, and P.V. Kamat, *Modulation of Cu_{2-x}S Nanocrystal Plasmon Resonance through Reversible Photoinduced Electron Transfer*. ACS nano, 2016. **10**(2): p. 2880-2886.
9. Mayer, K.M. and J.H. Hafner, *Localized surface plasmon resonance sensors*. Chemical reviews, 2011. **111**(6): p. 3828-3857.
10. Goel, S., F. Chen, and W. Cai, *Synthesis and biomedical applications of copper sulfide nanoparticles: from sensors to theranostics*. Small, 2014. **10**(4): p. 631-645.
11. Kang, X., Z. Mai, X. Zou, P. Cai, and J. Mo, *A sensitive nonenzymatic glucose sensor in alkaline media with a copper nanocluster/multiwall carbon nanotube-modified glassy carbon electrode*. Analytical biochemistry, 2007. **363**(1): p. 143-150.
12. Zhang, X., G. Wang, A. Gu, Y. Wei, and B. Fang, *CuS nanotubes for ultrasensitive nonenzymatic glucose sensors*. Chemical Communications, 2008(45): p. 5945-5947.
13. Zhuang, Z., X. Su, H. Yuan, Q. Sun, D. Xiao, and M.M. Choi, *An improved sensitivity non-enzymatic glucose sensor based on a CuO nanowire modified Cu electrode*. Analyst, 2008. **133**(1): p. 126-132.
14. Myung, Y., D.M. Jang, Y.J. Cho, H.S. Kim, J. Park, J.-U. Kim, Y. Choi, and C.J. Lee, *Nonenzymatic amperometric glucose sensing of platinum, copper*

sulfide, and tin oxide nanoparticle-carbon nanotube hybrid nanostructures.

The Journal of Physical Chemistry C, 2009. **113**(4): p. 1251-1259.

15. Jiang, L.-C. and W.-D. Zhang, *A highly sensitive nonenzymatic glucose sensor based on CuO nanoparticles-modified carbon nanotube electrode.* Biosensors and Bioelectronics, 2010. **25**(6): p. 1402-1407.
16. Li, C., Y. Su, S. Zhang, X. Lv, H. Xia, and Y. Wang, *An improved sensitivity nonenzymatic glucose biosensor based on a Cu x O modified electrode.* Biosensors and bioelectronics, 2010. **26**(2): p. 903-907.
17. Liu, J. and D. Xue, *Rapid and scalable route to CuS biosensors: a microwave-assisted Cu-complex transformation into CuS nanotubes for ultrasensitive nonenzymatic glucose sensor.* Journal of Materials Chemistry, 2011. **21**(1): p. 223-228.
18. Wang, A.-J., J.-J. Feng, Z.-H. Li, Q.-C. Liao, Z.-Z. Wang, and J.-R. Chen, *Solvothermal synthesis of Cu/Cu₂O hollow microspheres for non-enzymatic amperometric glucose sensing.* CrystEngComm, 2012. **14**(4): p. 1289-1295.
19. Zhang, Y., L. Su, D. Manuzzi, H.V.E. de los Monteros, W. Jia, D. Huo, C. Hou, and Y. Lei, *Ultrasensitive and selective non-enzymatic glucose detection using copper nanowires.* Biosensors and Bioelectronics, 2012. **31**(1): p. 426-432.
20. Qian, L., J. Mao, X. Tian, H. Yuan, and D. Xiao, *In situ synthesis of CuS nanotubes on Cu electrode for sensitive nonenzymatic glucose sensor.* Sensors and Actuators B: Chemical, 2013. **176**: p. 952-959.

21. Yang, Y.J., W. Li, and J. Zi, *Mechanistic study of glucose oxidation on copper sulfide modified glassy carbon electrode*. *Electrochemistry Communications*, 2013. **34**: p. 304-307.
22. Lee, H., S.W. Yoon, E.J. Kim, and J. Park, *In-situ growth of copper sulfide nanocrystals on multiwalled carbon nanotubes and their application as novel solar cell and amperometric glucose sensor materials*. *Nano Letters*, 2007. **7**(3): p. 778-784.
23. Bo, X., J. Bai, L. Wang, and L. Guo, *In situ growth of copper sulfide nanoparticles on ordered mesoporous carbon and their application as nonenzymatic amperometric sensor of hydrogen peroxide*. *Talanta*, 2010. **81**(1): p. 339-345.
24. Yang, Y.J., J. Zi, and W. Li, *Enzyme-free sensing of hydrogen peroxide and glucose at a CuS nanoflowers modified glassy carbon electrode*. *Electrochimica Acta*, 2014. **115**: p. 126-130.
25. Zou, J., J. Ma, Y. Zhang, L. Huang, and Q. Wan, *A hydroquinone sensor based on a new nanocrystals modified electrode*. *Journal of Chemical Technology and Biotechnology*, 2014. **89**(2): p. 259-264.
26. Zou, J., J. Ma, Y. Zhang, L. Li, J. Jiang, and J. Chen, *Electrochemical determination of pentachlorophenol using a glassy carbon electrode modified with a film of CuS nanocomposite-chitosan*. *Analytical Letters*, 2013. **46**(7): p. 1108-1116.
27. Ding, C., H. Zhong, and S. Zhang, *Ultrasensitive flow injection chemiluminescence detection of DNA hybridization using nanoCuS tags*. *Biosensors and Bioelectronics*, 2008. **23**(8): p. 1314-1318.

28. Zhang, S., H. Zhong, and C. Ding, *Ultrasensitive flow injection chemiluminescence detection of DNA hybridization using signal DNA probe modified with Au and CuS nanoparticles*. *Analytical chemistry*, 2008. **80**(19): p. 7206-7212.
29. Zhu, H., J. Wang, and G. Xu, *Fast synthesis of Cu₂O hollow microspheres and their application in DNA biosensor of hepatitis B virus*. *Crystal Growth and Design*, 2008. **9**(1): p. 633-638.
30. Ding, C., Z. Wang, H. Zhong, and S. Zhang, *Ultrasensitive chemiluminescence quantification of single-nucleotide polymorphisms by using monobase-modified Au and CuS nanoparticles*. *Biosensors and Bioelectronics*, 2010. **25**(5): p. 1082-1087.
31. Sagade, A.A. and R. Sharma, *Copper sulphide (Cu_xS) as an ammonia gas sensor working at room temperature*. *Sensors and Actuators B: Chemical*, 2008. **133**(1): p. 135-143.
32. Zhang, W., Z. Chen, and Z. Yang, *An inward replacement/etching route to synthesize double-walled Cu₇S₄ nanoboxes and their enhanced performances in ammonia gas sensing*. *Physical Chemistry Chemical Physics*, 2009. **11**(29): p. 6263-6268.
33. Fu, T., *CuS-doped CuO nanoparticles sensor for detection of H₂S and NH₃ at room temperature*. *Electrochimica Acta*, 2013. **112**: p. 230-235.
34. Xu, J., J. Zhang, C. Yao, and H. Dong, *Synthesis of Novel Highly Porous CuS Golf Balls by Hydrothermal Method and Their Application in Ammonia Gas Sensing*. *Journal of the Chilean Chemical Society*, 2013. **58**(2): p. 1722-1724.

35. Sun, N., Q. Guo, J. Shao, B. Qiu, Z. Lin, K. Wong, and G. Chen, *A signal-on fluorescence biosensor for detection of adenosine triphosphate based on click chemistry*. *Analytical Methods*, 2014. **6**(10): p. 3370-3374.
36. Chen, Z., Y. Lei, H. Xu, X. Chen, and J. Liu, *Functionalized gold nanorods as an immunosensor probe for neuron specific enolase sensing via resonance light scattering*. *Journal of Materials Chemistry B*, 2013. **1**(24): p. 3031-3034.
37. Samanta, A., Y. Zhou, S. Zou, H. Yan, and Y. Liu, *Fluorescence quenching of quantum dots by gold nanoparticles: a potential long range spectroscopic ruler*. *Nano letters*, 2014. **14**(9): p. 5052-5057.
38. Tian, F., F. Bonnier, A. Casey, A.E. Shanahan, and H.J. Byrne, *Surface enhanced Raman scattering with gold nanoparticles: effect of particle shape*. *Analytical Methods*, 2014. **6**(22): p. 9116-9123.
39. Khoury, C.G. and T. Vo-Dinh, *Gold nanostars for surface-enhanced Raman scattering: synthesis, characterization and optimization*. *The Journal of Physical Chemistry C*, 2008. **112**(48): p. 18849-18859.
40. Wustholz, K.L., A.-I. Henry, J.M. McMahon, R.G. Freeman, N. Valley, M.E. Piotti, M.J. Natan, G.C. Schatz, and R.P.V. Duyne, *Structure– activity relationships in gold nanoparticle dimers and trimers for surface-enhanced Raman spectroscopy*. *Journal of the American Chemical Society*, 2010. **132**(31): p. 10903-10910.
41. Chen, H., L. Shao, Q. Li, and J. Wang, *Gold nanorods and their plasmonic properties*. *Chemical Society Reviews*, 2013. **42**(7): p. 2679-2724.

42. Stewart, M.E., C.R. Anderton, L.B. Thompson, J. Maria, S.K. Gray, J.A. Rogers, and R.G. Nuzzo, *Nanostructured plasmonic sensors*. Chemical reviews, 2008. **108**(2): p. 494-521.
43. Willets, K.A. and R.P. Van Duyne, *Localized surface plasmon resonance spectroscopy and sensing*. Annu. Rev. Phys. Chem., 2007. **58**: p. 267-297.
44. Kruszynska, M., H. Borchert, A. Bachmatiuk, M.H. Rummeli, B. Büchner, J.r. Parisi, and J. Kolny-Olesiak, *Size and shape control of colloidal copper (I) sulfide nanorods*. ACS nano, 2012. **6**(7): p. 5889-5896.
45. Xie, Y., L. Carbone, C. Nobile, V. Grillo, S. D'Agostino, F. Della Sala, C. Giannini, D. Altamura, C. Oelsner, and C. Kryschi, *Metallic-like stoichiometric copper sulfide nanocrystals: phase-and shape-selective synthesis, near-infrared surface plasmon resonance properties, and their modeling*. ACS nano, 2013. **7**(8): p. 7352-7369.
46. Tsai, M.L., S.W. Bai, and R.H. Chen, *Cavitation effects versus stretch effects resulted in different size and polydispersity of ionotropic gelation chitosan–sodium tripolyphosphate nanoparticle*. Carbohydrate Polymers, 2008. **71**(3): p. 448-457.
47. Song, S., X. Zhou, L. Li, and W. Ma, *Numerical simulation and experimental validation of SiC nanoparticle distribution in magnesium melts during ultrasonic cavitation based processing of magnesium matrix nanocomposites*. Ultrasonics sonochemistry, 2015. **24**: p. 43-54.
48. Lin, X.Z., A.D. Terepka, and H. Yang, *Synthesis of silver nanoparticles in a continuous flow tubular microreactor*. Nano Letters, 2004. **4**(11): p. 2227-2232.

49. Wagner, J. and J. Köhler, *Continuous synthesis of gold nanoparticles in a microreactor*. Nano letters, 2005. **5**(4): p. 685-691.
50. Polte, J., R. Erler, A.F. Thunemann, S. Sokolov, T.T. Ahner, K. Rademann, F. Emmerling, and R. Kraehnert, *Nucleation and growth of gold nanoparticles studied via in situ small angle X-ray scattering at millisecond time resolution*. ACS nano, 2010. **4**(2): p. 1076-1082.
51. Edel, J.B. and R. Fortt, *Microfluidic routes to the controlled production of nanoparticles*. Chemical Communications, 2002(10): p. 1136-1137.
52. Wang, H., H. Nakamura, M. Uehara, M. Miyazaki, and H. Maeda, *Preparation of titania particles utilizing the insoluble phase interface in a microchannel reactor*. Chem. Commun., 2002(14): p. 1462-1463.
53. Chan, E.M., R.A. Mathies, and A.P. Alivisatos, *Size-controlled growth of CdSe nanocrystals in microfluidic reactors*. Nano Letters, 2003. **3**(2): p. 199-201.
54. Song, Y., H. Modrow, L.L. Henry, C.K. Saw, E. Doomes, V. Palshin, J. Hormes, and C.S. Kumar, *Microfluidic synthesis of cobalt nanoparticles*. Chemistry of materials, 2006. **18**(12): p. 2817-2827.
55. Song, Y., L.L. Henry, and W. Yang, *Stable amorphous cobalt nanoparticles formed by an in situ rapidly cooling microfluidic process*. Langmuir, 2009. **25**(17): p. 10209-10217.
56. Luan, W., H. Yang, N. Fan, and S.-T. Tu, *Synthesis of efficiently green luminescent CdSe/ZnS nanocrystals via microfluidic reaction*. Nanoscale Research Letters, 2008. **3**(4): p. 134-139.

57. Wang, H., X. Li, M. Uehara, Y. Yamaguchi, H. Nakamura, M. Miyazaki, H. Shimizu, and H. Maeda, *Continuous synthesis of CdSe–ZnS composite nanoparticles in a microfluidic reactor*. Chem. Commun., 2004(1): p. 48-49.
58. Song, Y., J. Hormes, and C.S. Kumar, *Microfluidic synthesis of nanomaterials*. Small, 2008. **4**(6): p. 698-711.
59. Li, Y., A. Sanampudi, V. Raji Reddy, S. Biswas, K. Nandakumar, D. Yemane, J. Goettert, and C.S. Kumar, *Size evolution of gold nanoparticles in a millifluidic reactor*. ChemPhysChem, 2012. **13**(1): p. 177-182.
60. Biswas, S., J.T. Miller, Y. Li, K. Nandakumar, and C.S. Kumar, *Developing a millifluidic platform for the synthesis of ultrasmall nanoclusters: ultrasmall copper nanoclusters as a case study*. Small, 2012. **8**(5): p. 688-698.
61. Zhao, C.-X., L. He, S.Z. Qiao, and A.P. Middelberg, *Nanoparticle synthesis in microreactors*. Chemical Engineering Science, 2011. **66**(7): p. 1463-1479.
62. Hassan, A.A., O. Sandre, V. Cabuil, and P. Tabeling, *Synthesis of iron oxide nanoparticles in a microfluidic device: preliminary results in a coaxial flow millichannel*. Chemical Communications, 2008(15): p. 1783-1785.
63. Li, Y., D.G. Yamane, S. Li, S. Biswas, R.K. Reddy, J.S. Goettert, K. Nandakumar, and C.S. Kumar, *Geometric optimization of liquid–liquid slug flow in a flow-focusing millifluidic device for synthesis of nanomaterials*. Chemical engineering journal, 2013. **217**: p. 447-459.
64. Kanehara, M., H. Koike, T. Yoshinaga, and T. Teranishi, *Indium tin oxide nanoparticles with compositionally tunable surface plasmon resonance frequencies in the near-IR region*. Journal of the American Chemical Society, 2009. **131**(49): p. 17736-17737.

65. Jun, H., T. Fabienne, M. Florent, P.-E. Coulon, M. Nicolas, and S. Olivier, *Understanding of the size control of biocompatible gold nanoparticles in millifluidic channels*. Langmuir, 2012. **28**(45): p. 15966-15974.
66. Lohse, S.E., J.R. Eller, S.T. Sivapalan, M.R. Plews, and C.J. Murphy, *A simple millifluidic benchtop reactor system for the high-throughput synthesis and functionalization of gold nanoparticles with different sizes and shapes*. ACS nano, 2013. **7**(5): p. 4135-4150.
67. Tadmouri, R., M. Romano, L. Guillemot, O. Mondain-Monval, R. Wunenburger, and J. Leng, *Millifluidic production of metallic microparticles*. Soft Matter, 2012. **8**(41): p. 10704-10711.
68. Gottesman, R., A. Tangy, I. Oussadon, and D. Zitoun, *Silver nanowires and nanoparticles from a millifluidic reactor: application to metal assisted silicon etching*. New Journal of Chemistry, 2012. **36**(12): p. 2456-2459.
69. Lim, J.-M., A. Swami, L.M. Gilson, S. Chopra, S. Choi, J. Wu, R. Langer, R. Karnik, and O.C. Farokhzad, *Ultra-high throughput synthesis of nanoparticles with homogeneous size distribution using a coaxial turbulent jet mixer*. ACS nano, 2014. **8**(6): p. 6056-6065.
70. Jahn, A., J.E. Reiner, W.N. Vreeland, D.L. DeVoe, L.E. Locascio, and M. Gaitan, *Preparation of nanoparticles by continuous-flow microfluidics*. Journal of Nanoparticle Research, 2008. **10**(6): p. 925-934.
71. Chen, H., X. Kou, Z. Yang, W. Ni, and J. Wang, *Shape-and size-dependent refractive index sensitivity of gold nanoparticles*. Langmuir, 2008. **24**(10): p. 5233-5237.

72. Nath, N. and A. Chilkoti, *Label-free biosensing by surface plasmon resonance of nanoparticles on glass: optimization of nanoparticle size*. Analytical Chemistry, 2004. **76**(18): p. 5370-5378.
73. Zeng, S., X. Yu, W.-C. Law, Y. Zhang, R. Hu, X.-Q. Dinh, H.-P. Ho, and K.-T. Yong, *Size dependence of Au NP-enhanced surface plasmon resonance based on differential phase measurement*. Sensors and Actuators B: Chemical, 2013. **176**: p. 1128-1133.
74. Weng, C.-H., C.-C. Huang, C.-S. Yeh, H.-Y. Lei, and G.-B. Lee, *Synthesis of hexagonal gold nanoparticles using a microfluidic reaction system* Preliminary results of the current paper were presented at the 7th Annual IEEE International Conference on Nanotechnology (Hong Kong, 2–5 August 2007)(IEEE NANO 2007). Journal of Micromechanics and microengineering, 2008. **18**(3): p. 035019.
75. Bird, R.B., W.E. Stewart, and E.N. Lightfoot, *Transport phenomena*. 2007: John Wiley & Sons.
76. Guo, M., W.-C. Law, X. Liu, H. Cai, L. Liu, M.T. Swihart, X. Zhang, and P.N. Prasad, *Plasmonic semiconductor nanocrystals as chemical sensors: Pb²⁺ quantitation via aggregation-induced plasmon resonance shift*. Plasmonics, 2014. **9**(4): p. 893-898.
77. Jain, P.K., K. Manthiram, J.H. Engel, S.L. White, J.A. Faucheaux, and A.P. Alivisatos, *Doped Nanocrystals as Plasmonic Probes of Redox Chemistry*. Angewandte Chemie International Edition, 2013. **52**(51): p. 13671-13675.

78. Guan, J., J. Peng, and X. Jin, *Synthesis of copper sulfide nanorods as peroxidase mimics for the colorimetric detection of hydrogen peroxide*. *Analytical Methods*, 2015. **7**(13): p. 5454-5461.
79. Sun, J., B. Wang, X. Zhao, Z.-J. Li, and X. Yang, *Fluorescent and Colorimetric Dual-Readout Assay for Inorganic Pyrophosphatase with Cu²⁺-Triggered Oxidation of o-Phenylenediamine*. *Analytical chemistry*, 2015.
80. Vedamalai, M., A.P. Periasamy, C.-W. Wang, Y.-T. Tseng, L.-C. Ho, C.-C. Shih, and H.-T. Chang, *Carbon nanodots prepared from o-phenylenediamine for sensing of Cu²⁺ ions in cells*. *Nanoscale*, 2014. **6**(21): p. 13119-13125.
81. Li, W., R. Zamani, P. Rivera Gil, B. Pelaz, M. Ibáñez, D. Cadavid, A. Shavel, R.A. Alvarez-Puebla, W.J. Parak, and J. Arbiol, *CuTe nanocrystals: shape and size control, plasmonic properties, and use as SERS probes and photothermal agents*. *Journal of the American Chemical Society*, 2013. **135**(19): p. 7098-7101.
82. Christopher, G. and S. Anna, *Microfluidic methods for generating continuous droplet streams*. *Journal of Physics D: Applied Physics*, 2007. **40**(19): p. R319.
83. Saldanha, P.L., R. Brescia, M. Prato, H. Li, M. Povia, L. Manna, and V. Lesnyak, *Generalized one-pot synthesis of copper sulfide, selenide-sulfide, and telluride-sulfide nanoparticles*. *Chemistry of Materials*, 2014. **26**(3): p. 1442-1449.
84. Jägeler-Hoheisel, T., J. Cordeiro, O. Lecarme, A.I. Cuche, C. Girard, E. Dujardin, D. Peyrade, and A. Arbouet, *Plasmonic shaping in gold*

- nanoparticle three-dimensional assemblies*. The Journal of Physical Chemistry C, 2013. **117**(44): p. 23126-23132.
85. Albella, P., B. Garcia-Cueto, F. González, F. Moreno, P.C. Wu, T.-H. Kim, A. Brown, Y. Yang, H.O. Everitt, and G. Videen, *Shape matters: plasmonic nanoparticle shape enhances interaction with dielectric substrate*. Nano letters, 2011. **11**(9): p. 3531-3537.
86. Zuber, A., M. Purdey, E. Schartner, C. Forbes, B. van der Hoek, D. Giles, A. Abell, T. Monro, and H. Ebendorff-Heidepriem, *Detection of gold nanoparticles with different sizes using absorption and fluorescence based method*. Sensors and Actuators B: Chemical, 2016. **227**: p. 117-127.